Climate Change from Short-Lived Emissions Due to Human Activities

Lead Authors: Drew T. Shindell, NASA/GISS; Hiram Levy II, NOAA/GFDL; Alice Gilliland, NOAA/ARL; M. Daniel Schwarzkopf, NOAA/GFDL; Larry W. Horowitz, NOAA/GFDL

Contributing Author: Jean-Francois Lamarque, NCAR

QUESTIONS AND ANSWERS

This chapter addresses the four questions regarding short-lived gases and particles that were posed in the Prospectus for this report:

Q5. What are the impacts of the radiatively active short-lived species (gases and particles) not explicitly the subject of prior CCSP assessments (SAP 2.1a: Scenarios of Greenhouse Gas Emissions and Atmospheric Concentrations)?

A5. Uncertainties in emissions projections for short-lived gases and particles are very large, even for a particular storyline. For particles, these uncertainties are usually dominant, while for tropospheric ozone, uncertainties in physical processes are more important. Differences among modeled future atmospheric burdens and radiative forcing for particles are dominated by divergent assumptions about emissions from South and East Asia. Particle mixing, particle indirect effects, the influence of ecosystem-chemistry interactions on methane, and stratosphere-troposphere exchange all contribute to large uncertainties separate from the emissions projections.

Q6. How do the impacts on climate of short-lived gases and particles compare with those of the well-mixed greenhouse gases as a function of the time horizon examined?

A6. By 2050 in two of the three models, changes in short-lived gas and particle concentrations (which are not reported in SAP 2.1a stabilization emission scenarios [Clarke et al., 2007]) contribute approximately 20 percent of global-mean annual-average warming, while one model shows virtually no effect. To a large extent, the inter-model differences are related to differences in emissions. Changes in the levels of short-lived gases and particles may play a substantial role out to 2100. One model finds that they can contribute 40 percent of the total projected summertime warming in the central United States over the second half of the 2100 century.

Q7. How do the regional impacts of short-lived species (gases and particles) compare with those of long-lived gases in or near polluted areas?

A7. The spatial distribution of radiative forcing is generally less important than the spatial distribution of climate response in predicting the impact on climate. Thus, both short-lived and long-lived gases and particles appear to cause enhanced climate responses in the same regions, rather than short-lived gases and particles having an enhanced effect primarily in or near polluted areas.

Q8. What might be the climate impacts of mitigation actions taken to reduce the atmospheric levels of short-lived species (gases and particles) to address air quality issues?

A8. Regional air quality emissions control strategies for short-lived pollutants have the potential to substantially affect climate globally. In one study, emissions reductions in the domestic energy/power sector in developing Asia, and to a lesser extent in the surface transportation sector in North America, appear to offer the greatest potential for substantial, simultaneous improvement in local air quality and mitigation of global warming.

3.1 INTRODUCTION

In this chapter, we describe results from numerical simulations of twenty-first century climate, with a major focus on the effects of short-lived gases and particles. The calculations incorporate results from three different types of models:

1. Integrated assessment models that produce emissions scenarios for particles and for ozone and particle precursors.
2. Global chemical composition models, which employ these emissions scenarios to generate concentrations for the short-lived radiatively active gases and particles.
3. Global comprehensive climate models, which calculate the climate response to the projected concentrations of both the short-lived and long-lived gases and particles. Box 1.1 outlines this sequence in detail.

Uncertainties in emissions projections for short-lived gases and particles are very large, even for a particular storyline.

The second part of Chapter 3, Section 3.2, is a discussion of the emissions scenarios and the models used to generate them, and the chemical composition models (sometimes called chemical transport models) used to produce the global distributions of short-lived gases and particles that help to drive the comprehensive climate models. Section 3.2 shows that, beginning with a single socioeconomic scenario for the time evolution of long-lived (well-mixed) greenhouse gases, different assumptions about the evolution of the particles and precursor gases lead to very different estimates of particle and ozone concentrations for the twenty-first century. We conclude that uncertainties in emissions projections for short-lived gases and particles are very large, even for a particular storyline. For particles, these uncertainties are usually dominant, while for tropospheric ozone, uncertainties in physical processes are more important.

The third part of Chapter 3, Section 3.3, discusses the three global comprehensive climate models (Geophysical Fluid Dynamics Laboratory [GFDL]; Goddard Institute for Space Studies [GISS]; Community Climate System Model [CCSM] developed in part at the National Center for Atmospheric Research [NCAR]) that have been used to calculate the impact of the short- and long-lived gases and particles[1] on the climate, focusing on the changes in surface temperature and precipitation. Supplementing the climate model results are calculations of the changes in radiative forcing[2] of the earth-atmosphere system. We find that by 2050, two of the three climate models show that approximately 20 percent of the global-mean annual-average warming is due to changing levels of radiatively active short-lived gases and particles. One model shows virtually no effect from short-lived gases and particles. To a large extent, the inter-model differences are related to differences in emissions. An extensive discussion and comparison of the projected distributions of short-lived species and resulting radiative forcings employed by the three groups and the resulting climate projections from the three comprehensive climate models can be found in Shindell *et al.* (2008).

One of the models has been extended to 2100. In that model, short-lived gases and particles play a substantial role, relative to the well-mixed greenhouse gases, in the surface temperature evolution out to 2100 and are responsible for 40 percent of the projected 2100 summertime warming in the central United States (Levy *et al.*, 2008).

The fourth part of Chapter 3, Section 3.4, discusses the effects of changes in regional particle and ozone and particle precursor emissions, using models that separate emissions by economic sector. The results show that regional air quality emissions control strategies for short-lived pollutants have the potential to substantially affect climate at large-scales. Emissions reductions from domestic sources in Asia, and to a lesser extent from surface transportation in North

[1] We distinguish here between short-lived gases and particles (which have atmospheric lifetimes less than one month and are non-uniformly distributed) and long-lived gases (which have lifetimes of a decade or more and are generally well mixed in the atmosphere).

[2] Radiative forcing is a measure of how the energy balance of the Earth-atmosphere system is influenced when factors that affect climate, such as atmospheric composition or surface reflectivity, are altered. When radiative forcing is positive, the energy of the Earth-atmosphere system will ultimately increase, leading to a warming of the system. In contrast, for a negative radiative forcing, the energy will ultimately decrease, leading to a cooling of the system. For technical details, see Box 3.2.

America, appear to offer the greatest potential for substantial, simultaneous improvement in local air quality and mitigation of global climate change.

3.2 EMISSIONS SCENARIOS AND COMPOSITION MODEL DESCRIPTIONS

3.2.1 Emissions Scenarios

The long-lived (well-mixed) greenhouse gases included in this study were carbon dioxide (CO_2), nitrous oxide (N_2O), methane (CH_4), and the minor gases (chlorofluorocarbons, sulfur hexafluoride). Projected global mean values were prescribed following the A1B "marker" storyline emissions scenario for all three modeling groups. Emissions for anthropogenic sources of particles and precursor gases and particles for all three composition model calculations were based on an international emissions inventory maintained in the Netherlands (Olivier and Berdowski, 2001).

Though the three groups in this study all prescribed future emissions following a specific socioeconomic scenario (A1B) that was highly studied in the Fourth Assessment by the Intergovernmental Panel on Climate Change (IPCC, 2007), they used different emissions trends for the short-lived gases and particles. There are several reasons for the differences. For one, the A1B emissions projections only provide estimates of anthropogenic emissions, and each model used its own natural emissions (though these were largely held constant). Secondly, integrated assessment models, while using the same socio-economic storyline (A1B), provided a range of emissions results (Nakićenović and Swart, 2000).

Two groups, GFDL and NCAR, used output from the AIM integrated assessment model (integrated assessment models are defined in Chapter 2, Section 2.1) while GISS used results from the IMAGE model. Though the emissions output generated from AIM was denoted the "marker" scenario by the IPCC, it was noted that it did not represent the average, best, or median result, and that all integrated assessment model results should be treated equally. Finally, emissions for some gases and particles, such as carbonaceous particles, were not provided.

This last issue motivated the GISS choice of the IMAGE model output, as it provided sufficient regional detail to allow carbonaceous particle emissions to be estimated consistently with the other gases and particles. Another complexity was the treatment of biomass burning emissions, which are partly natural and partly anthropogenic. In the GFDL model, biomass-burning emissions were assumed to be half anthropogenic and half natural. The GISS model instead used biomass burning emissions projections from another inventory (Streets *et al.*, 2004).

The result is a substantial divergence in the projected trends among the three models (Figure 3.1, Table 3.1). For sulfur dioxide (SO_2), the precursor to sulfate particle, the emissions follow reasonably similar trajectories, with globally averaged increases until 2030 followed by decreases to 2050 and even further decreases to 2100. However, the percentage increase is roughly double for GISS and CCSM as compared with GFDL. Thus even two composition models using anthropogenic emissions projections from the same integrated assessment model show large differences in the evolution of their total emissions, presumably owing to differences in the present-day emissions inventories. At 2050, the GFDL model has substantially reduced emissions compared with 2000, while the other models show enhanced emissions relative to 2000. A similar divergence in projected sulfur-dioxide trends is present in the SAP 2.1a stabilization emissions scenarios (Clarke *et al.*, 2007) discussed in Chapter 2, with emissions decreasing dramatically (~70 percent) by

Though the three groups in this study all prescribed future emissions following a specific socioeconomic scenario, the scenario has multiple interpretations, and hence they used different emissions trends for the short-lived gases and particles.

Table 3.1 Global emissions. Emissions (in Teragrams, Tg = 1 x 10^{12} g) include both natural and anthropogenic sources. Values in parentheses are changes relative to 2000.

Species	Model	2000	2030	2050	2100
NO_x (Tg N per year)	GFDL	40	57 (43%)	54 (35%)	48 (20%)
	GISS	50.5	67.0 (33%)	77.5 (53%)	NA
BC (Tg C per year)	GFDL	10.9	14.0 (28%)	15.3 (40%)	19.9 (83%)
	GISS	8.6	6.8 (-21%)	6.0 (-30%)	NA
OC (Tg C per year)	GFDL	51.5	61.9 (20%)	66.5 (29%)	84.3 (%)
	GISS	69.5	57.0 (-18%)	58.3 (-16%)	NA
SO_2 (Tg SO_2 per year)	GFDL	147	187 (27%)	118 (-20%)	56 (-62%)
	GISS	130	202 (55%)	164 (26%)	NA
	CCSM	125	190 (52%)	148 (18%)	NA
Dust (Tg per year)	GFDL	2471	2471	2471	2471
	GISS	1580	1580	1580	NA

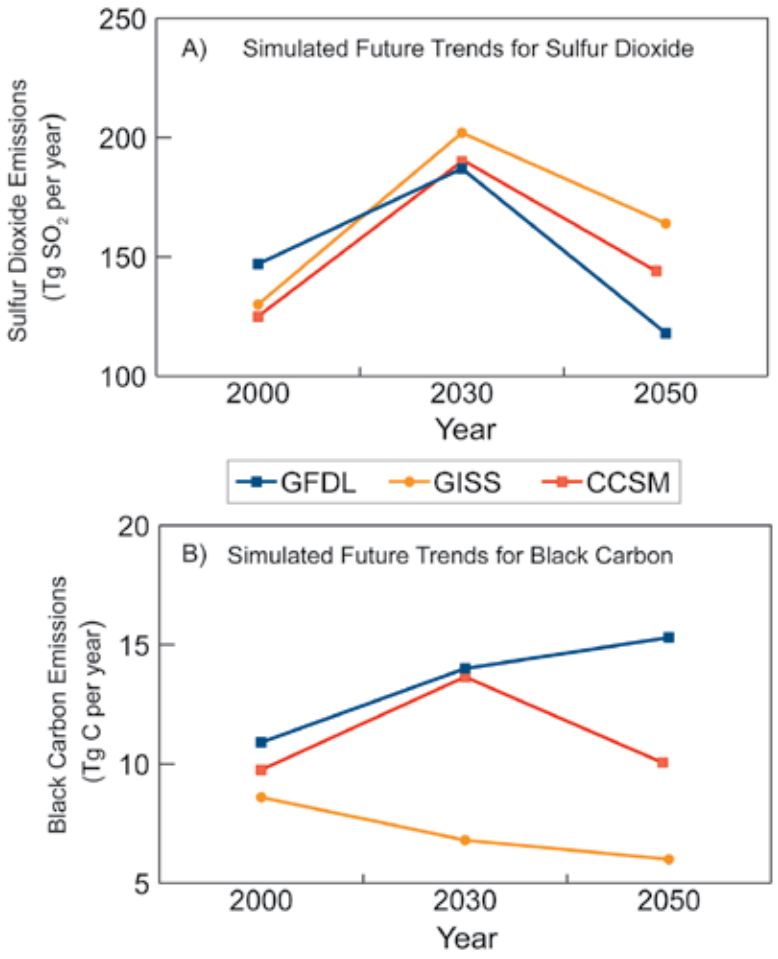

Figure 3.1 A1B emissions trends used in the three models for SO_2 (top) and black carbon (bottom). Note that in the CCSM model, the present day black carbon distribution was scaled in the future rather than calculated from black carbon emissions. Scaling was chosen to mimic the global sulfur dioxide emissions, a 40 percent increase over 2000 at 2030, and 10 percent at 2050. The CCSM 2000 black carbon global emission is set at the average of the GISS and GFDL 2000 values, and follows this scaling in the future, for illustrative purposes.

2050 in one integrated assessment model (MINICAM) while decreasing only moderately (~20 percent) in the two others, and even beginning to increase again after about 2040 in one of those two.

Differences are even more striking for carbonaceous particle emissions, which were not provided by any of the integrated assessment models. We focus on black carbon (BC) as the more important radiative perturbation. For this particle (and for organic carbon [OC]), the GFDL composition model uses the IPCC recommendation to scale carbonaceous particle emissions to carbon monoxide emissions, leading to substantial increases with time (Figure 3.1, Table 3.1). However, many of the sources of carbon monoxide emissions are different from those of carbonaceous particles. The NCAR group did not simulate the future composition of black and organic carbon based on emissions projections, but instead scaled their present-day distribution by the global factors derived for sulfur dioxide. The time evolution of black and organic carbon emissions in the CCSM model thus follows the same trajectory as that of SO_2. On the other hand, the GISS group used emissions projections from Streets *et al.* (2004) based on energy and fuel usage trends from the IMAGE model (as for other gases and particles) and including expected changes in technology. This led to a substantial reduction in future emissions of carbonaceous particles.

For precursors of tropospheric ozone, there was again divergence among the models. The primary precursor in most regions, NO_x (nitrogen oxides = NO + NO_2), increased steadily in the projections used by GISS, while it peaked at 2030 and decreased slightly thereafter in the projections used at GFDL (Table 3.1). Hydrocarbons and carbon monoxide show analogous differences. Methane was prescribed according to the A1B "marker" scenario values for all three composition models. Thus ozone, in addition

to the particles, was modeled in substantially different ways at the three centers.

The three models included projected changes in the same gases and particles, with the exception of nitrate, which only varied in the GISS model. As its contribution to total particle and total particle radiative forcing is small, at least in this GISS model, this particular difference was not significant in our results.

3.2.2 Composition Models

The chemical composition models used to produce short-lived gas and particle concentrations for the GFDL, GISS, and CCSM climate models were driven by the emissions projections discussed in Section 3.2.1. While the three models did not use identical present-day emissions, their anthropogenic emissions were based on the same international inventory (Olivier and Berdowski, 2001). The chemical composition simulations were run for one or two years, with the three-dimensional monthly mean concentrations and optical properties archived for use as off-line concentration fields to drive the climate model simulations discussed in Section 3.3. These simulations were all performed with present-day meteorology (values for temperature, moisture, and wind). Further details about the chemical composition models are provided in Appendix C.

3.2.2.1 Geophysical Fluid Dynamics Laboratory (GFDL)

Composition changes for the short-lived gases and particles in the GFDL experiments were calculated using the global chemical transport model MOZART-2 (Model for OZone And Related chemical Tracers, version 2.4), which has been described in detail previously (Horowitz *et al.*, 2003; Horowitz, 2006; and references therein). This model was used to generate the monthly average distributions of tropospheric ozone, sulfate, and black and organic carbon as a function of latitude, longitude, altitude, and time for the emissions scenarios discussed above. Simulated ozone concentrations agree well with present-day observations and recent trends (Horowitz, 2006). Overall, the predicted concentrations of particle are within a factor of two of the observed values and have a tendency to be overestimated (Ginoux *et al.*, 2006). Further details on the MOZART model are found in Appendix C, in the section on Geophysical Fluid Dynamics Laboratory.

3.2.2.2 Goddard Institute for Space Studies (GISS)

The configuration of the GISS composition model used here has been described in detail in (Shindell *et al.*, 2007). In brief, the composition model PUCCINI (Physical Understanding of Composition-Climate INteractions and Impacts) includes ozone and oxidant photochemistry in both the troposphere and stratosphere (Shindell *et al.*, 2006b), sulfate, carbonaceous and sea-salt particles (Koch *et al.*, 2006, 2007), nitrate particles (Bauer *et al.*, 2007), and mineral dust (Miller *et al.*, 2006a). Present-day composition results in the model are generally similar to those in the underlying chemistry and particle models. Further details on the PUCCINI model resolution, composition, and performance are found in Appendix C, in the section on Goddard Institute for Space Studies.

While the three models used in this study did not use identical present-day emissions, their human-caused emissions were based on the same international inventory.

3.2.2.3 Community Climate System Model (CCSM)

For the climate simulations described in this section, present-day tropospheric ozone was taken from Lamarque *et al. (*2005a); beyond 2000, tropospheric ozone was calculated by T. Wigley using the MAGICC composition model <http://www.cru.uea.ac.uk/~mikeh/software/magicc.htm> forced by the time-varying emissions of NO_x, methane and volatile organic compounds (VOCs) and these average global values were used to scale the present-day distribution. Future carbonaceous particles are scaled from their present-day distribution (Collins *et al.*, 2001) by a globally uniform factor whose time evolution follows the global evolution of SO_2 emissions. Stratospheric ozone changes are prescribed following the study by (Kiehl *et al.*, 1999). Further details on the composition models used by NCAR are found in Appendix C in the section on National Center for Atmospheric Research.

3.2.3 Tropospheric Burden

The composition models each calculate time-varying three-dimensional distributions of the short-lived gases and particles (except for CCSM where 2030 and 2050 ozone, black carbon, and organic carbon were scaled based

Table 3.2 Global burdens. Values in parentheses are changes relative to 2000.

Species	Model	2000	2030	2050	2100
BC (Tg C)	GFDL	0.28	0.36 (29%)	0.39 (39%)	0.51
	GISS**	0.26	0.19 (-27%)	0.15 (-42%)	NA
	CCSM		(40%)	(10%)	
OC* (Tg C)	GFDL	1.35	1.59 (18%)	1.70 (26%)	2.15
	GISS	1.65	1.33 (-19%)	1.27 (-23%)	NA
	CCSM		(40%)	(10%)	
Sulfate (Tg $SO_4^=$)	GFDL	2.52	3.21 (27%)	2.48 (-2%)	1.50 (-40%)
	GISS	1.51	2.01 (33%)	1.76 (17%)	NA
	CCSM				
Dust (Tg)	GFDL	22.31	22.31	22.31	22.31
	GISS	34.84	34.84	34.84	NA
	CCSM				
Tropospheric Ozone (DU)	GFDL	34.0	38.4 (13%)	39.3 (16%)	38.2 (12%)
	GISS	31.6	41.5 (31%)	47.8 (51%)	NA
	CCSM	28.0	41.5 (48%)	43.0 (54%)	NA

*The organic carbon (OC) burdens include primary OC particles (with emissions as in Table 3.1) plus secondary OC particles (SOA). In the GFDL model, the global burden of SOA is 0.07 Tg C in this inventory. In the GISS model, organic carbon from SOA makes up ~24% of present-day OC emissions. Burdens are given in units of teragrams (1Tg = 1012 g) for particles and in units of Dobson units (1DU globally averaged = 10.9 Tg O3) for ozone.
**GISS sulfate burdens include sulfate on dust surfaces, which makes up as much as one-half the total burden.

The concentrations of sulfate and carbonaceous particles are all influenced by differences in how the models simulate removal by the hydrologic cycle, accounting for at least some of the 10 to 15 percent difference in residence times in the atmosphere.

on their 2000 distributions). We compare these using the simple metric of the global mean annual average tropospheric burden (*i.e.*, the total mass in the troposphere). As was the case with emissions, the differences between the outputs of the composition models are substantial (Table 3.2). The GFDL model has a 67 percent greater present-day burden of sulfate than the GISS model, for example. As the GFDL sulfur dioxide emissions were only 13 percent greater, this suggests that either sulfate stays in the air longer in the GFDL model than in the GISS model or sulfur dioxide is converted more efficiently to sulfate in the GFDL model.

This can be tested by analyzing the atmospheric residence times of the respective models (Table 3.3). The residence time of sulfate is within ~10 percent in the two models, and in fact is slightly less in the GFDL model. This indicates that the conversion of sulfur dioxide (SO_2) to sulfate must be much more efficient in the GFDL model for it to have a sulfate burden so much larger than the GISS model. This is clearly seen in the ratio between sulfate burden and SO_2 emissions (Table 3.4). This ratio can be analyzed in terms of the total sulfur dioxide burden (in Tg [teragrams]) per SO_2 emission (in Tg per yr); the change in SO_2 burden per SO_2 emission change, or alternatively in the percentage change in each. The latter is probably the most useful evaluation, as the fractional change will reduce differences between the starting points of the two models. We note that this metric is affected by both production and removal rates in the models. Table 3.4 shows clearly that the production of sulfate per Tg of sulfur emitted is much greater in the GFDL model than in the GISS model, either because of differences in other sources of sulfate (*e.g.*, from dimethyl sulfide [DMS]) or differences in the chemical conversion efficiency of SO_2 to sulfate (versus physical removal of SO_2 by deposition).

The residence times of black and organic carbon (BC and OC) are also fairly similar in these two models (Table 3.3). The concentrations of sulfate and carbonaceous particles are all influenced by differences in how the models simulate removal by the hydrologic cycle, accounting for at least some of the 10 to 15 percent difference in residence times. Sulfate production can vary even more from model to model, as its production from the emitted sulfur di-

Table 3.3 Global mean annual average particle residence times (days).

Species	Model	2000	2030	2050
BC	GFDL	9.4	9.4	9.3
	GISS	11.0	10.2	9.1
OC	GFDL	9.6	9.4	9.3
	GISS	8.7	8.5	8.0
Sulfate	GFDL	8.0	8.2	8.1
	GISS	8.8	8.8	9.0

oxide involves chemical oxidation, which can differ substantially between models. Removal of sulfur dioxide prior to conversion to sulfate may also be more efficient in the GISS model. In contrast, BC and OC are emitted directly, and hence any differences in how these are represented in the models would be apparent in their residence times.

The particle residence times are relatively stable in time in the GISS and GFDL models. The carbonaceous particle residence times do decrease with time in the GISS model (and to a lesser extent in the GFDL model for OC), probably owing to the shift with time from mid- to tropical latitudes, where wet and dry removal rates are different (more rapid net removal). The sulfate residence time is fairly stable over the 2000 to 2050 period. The ratio of sulfate burden to SO_2 emissions is the same for the present-day and the 2030 to 2000 changes in the GFDL model. For the 2100 to 2000 change in that model (not shown), the ratio drops from 1.00 to 0.65. As the total emissions of SO_2 decrease, a larger fraction of the sulfate production comes from DMS oxidation rather than from emitted SO_2. The conversion efficiency from SO_2 to sulfate also varies over time in the GISS model, decreasing to 2030 and increasing thereafter (inversely related to total sulfur dioxide emissions). This may reflect both non-linearities in production (via oxidation chemistry) and the changing spatial pattern of emissions.

After comparison of the inter-model variations in particle residence times and chemical conversion efficiencies with the variations in emissions trends, it is clear that the differences in the projected changes in particle burdens in the GISS and GFDL simulations are primarily attributable to the underlying differences in emissions. This is especially true for carbonaceous particles, for which the residence times are quite similar in the models. Even though there is a greater difference in sulfate burdens due to the variations in chemical conversion efficiency between the models, the emissions trends at 2050 relative to 2000 are of opposite sign in the two models and thus dominate the difference in the burden change. Thus, the GISS model projects a greater sulfate burden at 2050 than at 2000, but substantially reduced burdens of carbonaceous particles, while the GFDL model projects the opposite, both because of the underlying emissions projections.

It is clear that the differences in the projected changes in particle burdens simulated in the two models are primarily attributable to the underlying differences in emissions.

Table 3.4 Ratio of sulfate and ozone burdens to precursor emissions, global mean annual average.

Species	Model	2000 Tg burden/ Tg emission per year	2030 vs. 2000 Tg burden/ Tg emission per year	2030 vs. 2000 % burden/ % emission	2050 vs. 2000 % burden/ % emission
Sulfate	GFDL	0.017	0.017	1.00	0.08*
	GISS	0.012	0.007	0.60	0.65
Ozone	GFDL	7.19	2.24	0.32	0.44
	GISS	6.82	6.54	0.94	0.96

Ratios for sulfate are in Tg sulfate divided by Tg SO_2 per year emitted as SO_2. Ozone ratios are in Tg ozone divided by Tg N per year emitted as NO_x. Ozone values in Table 3.2 are converted to burden assuming 1 DU globally averaged = 10.9 Tg ozone. Burdens are given in units of Teragrams (Tg = 1×10^{12} g).
*The burden change was only 2 percent in this case, making the calculation unreliable.

Table 3.5 All-sky aerosol optical depth (550nm extinction).

Region	Particle Type	Model	2000	2030	2050	2100
Global	BC	GFDL	.0076	.0096	.0105	.0138
		GISS	.0045	.0034	.0028	NA
	Sulfate	GFDL	.1018	.1227	.0906	.0591
		GISS	.0250	.0312	.0278	NA
		CCSM	.048	.062	.052	NA
	Sea salt	GFDL	.0236	.0236	.0236	.0236
		GISS	.1065	.1080	.1050	NA
		CCSM	.018	.018	.018	NA
	Dust	GFDL	.0281	.0281	.0281	.0281
		GISS	.0372	.0389	.0387	NA
		CCSM	.0275	.0275	.0275	NA
	OC	GFDL	.0104	.0122	.0131	.0166
		GISS	.0166	.0135	.0130	NA
	Nitrate	GISS	.0054	.0057	.0060	NA
	Total	***GFDL***	***.1715***	***.1964***	***.1660***	***.1411***
		GISS	***.1959***	***.2007***	***.1934***	***NA***
		CCSM	***.116***	***.1392***	***.1206***	***NA***
Northern Hemisphere	BC	GFDL	.0109	.0147	.0161	.0209
		GISS	.0062	.0043	.0032	NA
	Sulfate	GFDL	.1509	.1766	.1038	.0694
		GISS	.0352	.0449	.0388	NA
		CCSM	.078**	.097**	.073**	NA
	Dust	GISS	.0600	.0642	.0615	NA
		GFDL	.0491	.0491	.0491	.0491
	Sea salt	GISS	.0630	.0619	.0647	NA
		GFDL	.0181	.0181	.0181	.0181
	Total	***GFDL***	***.2430***	***.2756***	***.2056***	***.1807***
		GISS	***.1910***	***.1985***	***.1907***	***NA***
		CCSM	***.1538***	***.1827***	***.1502***	***NA***
Southern Hemisphere	BC	GFDL	.0042	.0046	.0049	.0066
		GISS	.0029	.0026	.0023	NA
	Sulfate	GFDL	.0526	.0689	.0774	.0487
		GISS	.0148	.0175	.0170	NA
		CCSM	.052**	.062**	.075**	NA
	Dust	GISS	.0144	.0137	.0159	NA
		GFDL	.0071	.0071	.0071	.0071
	Sea salt	GISS	.1502	.1541	.1453	NA
		GFDL	.0291	.0291	.0291	.0291
	Total	***GFDL***	***.1000***	***.1171***	***.1263***	***.1015***
		GISS	***.1997***	***.2030***	***.1962***	***NA***
		CCSM	***.0779***	***.0957***	***.0910***	***NA***

**Total for sulfate plus sea salt.

The ozone burden in the lower atmosphere increases in the future in all three models.

The results for tropospheric ozone tell a different story. The ozone burden increases in the future in all three models, but the percentage increase relative to 2000 differs by more than a factor of three at 2030 (Table 3.2). Examining the ozone changes relative to the NO_x emissions changes, there are very large differences between the GFDL and GISS models (Table 3.4). This may reflect the influence of processes such as stratospheric ozone influx which is independent of NO_x emissions, as well as the roles of precursors such as carbon monoxide (CO) and hydrocarbons that also influence tropospheric ozone. In particular, the GISS model computed a large increase in the flux of ozone into the troposphere as the stratospheric ozone layer recovered, while the composition model used at GFDL held stratospheric ozone fixed and hence did not simulate similar large increases. In addition, there are well-known non-linearities in O_3-NO_x chemistry (Stewart *et al.*, 1977), and it has been shown that the ozone production efficiency can vary substantially with time (Lamarque *et al.*, 2005a; Shindell *et al.*, 2006a). Thus for tropospheric ozone, the differences in modeled changes of nearly a factor of three (13 *vs.* 33 percent increase) are much larger than the differences in the NO_x precursor emissions (33 *vs.* 43 percent increase).

3.2.4 Aerosol Optical Depth

The global mean present-day all-sky aerosol optical depth (AOD)[3] in the three models ranges from 0.12 to 0.20 (Table 3.5). This difference of almost a factor of two suggests that particles are contributing quite differently to the Earth's energy balance with space in these models. Observational constraints on the all-sky value are not readily available, as most of the extant measurement techniques are reliable only in clear-sky (cloud-free) conditions. Sampling clear-sky areas only, the GISS model's global total aerosol optical depth is 0.12 for 2000 (0.13 Northern Hemisphere, 0.10 Southern Hemisphere). This includes contributions from sulfate, carbonaceous, nitrate, dust, and sea-salt particles. The clear-sky observations give global mean values of ~0.135 (ground-based AERONET) or ~0.15 (satellite composites, including AVHRR or MODIS observations), though these have substantial limitations in their spatial and temporal coverage. The CCSM

[3] Aerosol optical depth is a measure of the fraction of radiation at a given wavelength absorbed or scattered by particles while passing through the atmosphere.

and GFDL models did not calculate clear-sky aerosol optical depth. Given that the all-sky values are larger, and substantially so in the GISS model (though this will depend upon the water uptake of particles), it seems clear that the values for CCSM would be too small compared with observations since even their all-sky values are lower than the estimate from observations. This may be related to CCSM's use of AVHRR data in assimilation of aerosol optical depth to create the CCSM climatology (Collins *et al.*, 2001, 2006), as that data appears to be low relative to MODIS observations, for example.

For all three models, there are large differences in the contributions of the various particles (Figure 3.2; Table 3.5). This is true even for GFDL and GISS models, with relatively similar all-sky global mean aerosol optical depths. More than half the aerosol optical depth in the GFDL model comes from sulfate, while this particle contributes only about one-eighth the aerosol optical depth in the GISS model. Instead, the GISS model's aerosol optical depth is dominated by the largely natural sea salt and dust particles, which together contribute 0.14 to the aerosol optical depth. These two particles contribute a much smaller aerosol optical depth in the CCSM and GFDL models, ~0.06 or less, with the differences with respect to GISS predominantly due to sea salt. The relative contribution from sulfate in the CCSM model looks similar to the GFDL model, with nearly half its aerosol optical depth coming from sulfate, but the magnitude is much smaller. It seems clear that the GFDL model's direct sulfate contribution is biased high (Ginoux *et al.*, 2006), while the GISS model's sulfate is biased low in this model version (Shindell *et al.*, 2007). However, the relative importance of the different particles is not well understood at present (Kinne *et al.*, 2006).

Large differences in the relative aerosol optical depth in the Northern Hemisphere and Southern Hemisphere are also apparent in the models (Table 3.5). The ratios of the present-day Northern Hemisphere to Southern Hemisphere total aerosol optical depths in the three models differ widely, with values of 2.43, 1.97, and 0.96 in the GFDL, CCSM, and GISS models, respectively. This clearly reflects the dominant contribution of sulfate to optical depth in the GFDL and CCSM models, as it has large anthropogenic Northern Hemisphere sources, and the dominance of sea salt in the GISS model, with its largest source being the Southern Ocean. While composite satellite data shows clearly greater aerosol optical depths in the Northern Hemisphere than the Southern Hemisphere, most satellite instruments lose coverage near the northern edge of the Southern Ocean (Kinne *et al.*, 2006). Unfortunately, quality-controlled networks such as AERONET provide virtually no ground-based data poleward of 45°S. Thus while it seems unlikely that the aerosol optical depth is larger in the Southern Hemisphere than the Northern Hemisphere, as in the GISS model, presently available data are not adequate to fully characterize this ratio, as aerosol optical depths over the Southern Ocean are poorly known.

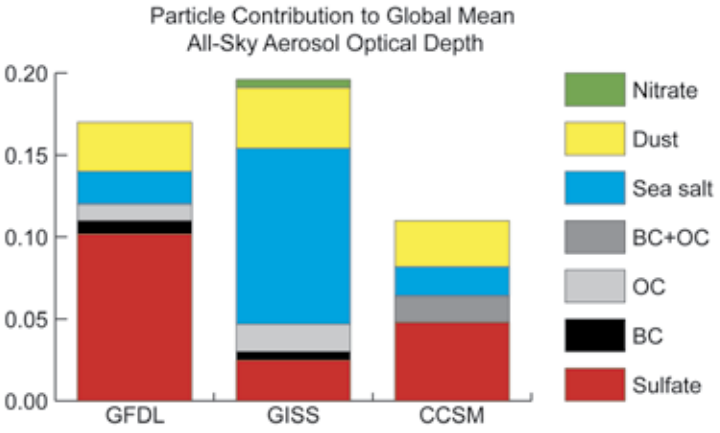

Figure 3.2 Present-day contributions from individual particles to global mean all-sky aerosol optical depth (550 nm). Neither GFDL nor CCSM include nitrate.

3.3 CLIMATE STUDIES

3.3.1 Experimental Design

The model experiments used here are designed to isolate the climate effects of projected changes in the short-lived gases and particles and calculate their importance relative to that of the long-lived well-mixed greenhouse gases.

The climate studies discussed here consist of transient climate simulations that were designed to isolate the climate effects of projected changes in the short-lived gases and particles and calculate their importance relative to that of the long-lived well-mixed greenhouse gases. The simulations from the GFDL, GISS, and NCAR groups each employed ensembles (multiple simulations differing only in their initial conditions) in order to reduce the unforced variability in the chaotic climate system. One three-member ensemble included the evolution of short- and long-lived gases and particles following the A1B storyline emission scenario, while the second ensemble included only the evolution of long-lived gases with the short-lived gases and particles fixed at present values. While all three groups used the same values for the long-lived gases, each had its own version of an A1B scenario for short-lived gases and particles, as discussed previously in Section 3.2.

The global three-dimensional distributions of short-lived gases and particles were modeled using each group's chemistry-particle composition model. For the first ensemble, the GFDL simulations used particle and ozone distributions computed each decade out to 2100, while the GISS and CCSM simulations employed values computed for 2000, 2030, and 2050. Either seasonally varying or monthly-average three-dimensional distributions were saved. Short-lived gas and particle concentrations for intermediate years were linearly interpolated between the values for computed years. In both sets of simulations, the concentrations of long-lived gases varied with time. In practice, NCAR performed only a single pair of simulations out to 2050, while GISS performed all three pairs out to 2050, and GFDL extended all three pairs out to 2100.

3.3.2 Climate Models

3.3.2.1 Geophysical Fluid Dynamics Laboratory (GFDL)

Climate simulations at GFDL used the comprehensive climate model (Atmosphere-Ocean General Circulation Model [AOGCM] [Box 1.1]) recently developed at NOAA's Geophysical Fluid Dynamics Laboratory, which is described in detail in Delworth *et al.* (2006). The control simulation of this AOGCM (using present-day values of radiatively active gases and particles) has a stable, realistic climate when integrated over multiple centuries. The model is able to capture the main features of the global evolution of observed surface temperature for the twentieth century as well as many continental-scale features (Knutson *et al.*, 2006). Its equilibrium climate sensitivity to a doubling of CO_2 is 3.4°C[4] (Stouffer *et al.*, 2006). The model includes the radiative effects of well-mixed gases and ozone on the climate as well as the direct effects of particles, but does not include the indirect particle effects (Box 3.1). Further details on the model resolution, model physics, and model performance are included in Appendix D in the section on Geophysical Fluid Dynamics Laboratory.

3.3.2.2 Goddard Institute for Space Studies (GISS)

The GISS climate simulations were performed using GISS ModelE (Schmidt *et al.*, 2006). This model has been extensively evaluated against observations (Schmidt *et al.*, 2006), and has a climate sensitivity in accord with values inferred from paleoclimate data and similar to that of mainstream General Circulation Models; the equilibrium climate sensitivity for doubled CO_2 is 2.6°C. The radiatively active compounds in the model include well-mixed gases, ozone, and particles. The model includes a simple parameterization for the particle indirect effect (Menon *et al.*, 2002) (Box 3.1). Further details on the model resolution and model physics are included in Appendix D in the section on Goddard Institute for Space Studies.

3.3.2.3 Community Climate System Model (CCSM)

The transient climate simulations use the CCSM Community Climate System Model CCSM3 (Collins *et al.*, 2006). The equilibrium climate sensitivity of this model to doubled CO_2 is 2.7°C. Further details on the model resolution

[4] Equilibrium climate sensitivity is defined here as the global-mean, annual-mean surface temperature change of a climate model in response to a doubling of atmospheric carbon dioxide from preindustrial levels, when the model has fully adjusted to the change in carbon dioxide.

BOX 3.1: Radiative Effects of Particles

The direct effects of particles refer to their scattering and absorption of both incoming solar and outgoing terrestrial radiation. By reflecting incoming radiation back to space, most particles have a negative radiative forcing (cooling effect). For reflective particles (sulfate, organic carbon, nitrate, dust and sea salt), this effect dominates over their absorption of outgoing radiation (the greenhouse effect) on the global scale. The balance varies both geographically and seasonally as a function of solar radiation and the ground temperature. In contrast, absorbing particles such as black carbon have a positive radiative forcing (warming effect) as they absorb incoming and outgoing radiation, reducing the overall fraction of the sun's irradiance that it reflected back to space. They can also absorb outgoing radiation from the Earth (the greenhouse effect).

In addition to their direct radiative effects, particles may also lead to an indirect radiative forcing of the climate system through their effect on clouds. Two particle indirect effects are identified: The first indirect effect (also known as the cloud albedo effect) occurs when an increase in particles causes an increase in cloud droplet concentration and a decrease in droplet size for fixed liquid water content (Twomey, 1974). Having more, smaller drops increases the cloud albedo (reflectivity). The second indirect effect (also known as the cloud lifetime effect) occurs when the reduction in cloud droplet size affects the precipitation efficiency, tending to increase the liquid water content, the cloud lifetime (Albrecht, 1989), and the cloud thickness (Pincus and Baker, 1994). As the clouds last longer, this leads to an increase in cloud cover. It has been argued that empirical data suggest that the second indirect effect is the dominant process (Hansen *et al.*, 2005).

Satellite- and ground-based observations have been used to estimate particle indirect effects and to evaluate their treatment in climate models (*e.g.*, Kaufmann *et al.*, 2005; Lohmann and Lesins, 2002). The recently available CALIPSO and CloudSat measurements, which provide vertical distributions of particles and clouds, may be particularly useful for these purposes. However, the difficulty of separating the influence of particle indirect effects from dynamical and meteorological effects remains a major problem for such observational studies (Lohmann *et al.*, 2006).

The direct effects of particles are relatively well-represented in climate models such as those described in Section 3.3.2 and used in this study, though substantial uncertainties exist regarding the optical properties of some particle types and especially of particle mixtures. Because of the inherent complexity of the particle indirect effect, climate model studies dealing with its quantification necessarily include an important level of simplification. While this represents a legitimate approach, it should be clear that the climate model estimates of the particle indirect effect are very uncertain.

The studies discussed in Chapter 3 of this Report include the direct effects of particles in all three models (though nitrate is only included in the GISS model). The indirect effect is only included in the GISS model, which uses a highly simplified representation of the second indirect effect.

and construction are found in Appendix D in the section on National Center for Atmospheric Research.

3.3.3 Radiative Forcing Calculations

The radiative forcing at the tropopause provides a useful, though limited, indicator of the climate response to perturbations (Hansen *et al.*, 2005) (Box 3.2).

3.3.3.1 Global and Hemispheric Average Values: GFDL and GISS

Radiative forcing calculations were performed by GFDL (adjusted forcing) and GISS (instantaneous forcing), but were not performed for the CCSM model. The annual-average global-mean radiative forcing (RF) from short-lived gases and particles at 2030 relative to 2000 is small in both the GFDL and GISS models (Figure 3.3;

BOX 3.2: Radiative Forcing

Radiative forcing is defined as the change in net (down minus up) irradiance (solar plus longwave, in W per m^2) at the tropopause due to a perturbation after allowing for stratospheric temperatures to adjust to radiative equilibrium, but with surface and tropospheric temperatures and state held fixed at the unperturbed values (IPCC, 2007; Ramaswamy *et al.*, 2001). This quantity is also sometimes termed adjusted radiative forcing. If the stratospheric temperatures are not allowed to adjust, the irradiance change is termed instantaneous radiative forcing.

The utility of the radiative forcing concept is that, to first order, the equilibrium global-mean, annual-mean surface temperature change is proportional to the radiative forcing, for a wide range of radiative perturbations. The proportionality constant (often denoted as the climate sensitivity parameter, λ) is approximately the same (to within 25 percent) for most drivers of climate change (IPCC, 2007), with a typical value of ~0.5-0.7 for most models. This enables a readily calculable and comparable measure of the climate response to radiative perturbations, such as those discussed in this Chapter.

Table 3.6). However, this is for quite different reasons. In the GFDL model, a large increase in sulfate optical depth leads to a negative forcing that is largely balanced by positive forcings from increased black carbon particle and ozone. In the GISS model, increased sulfate and reduced black carbon both lead to relatively small negative forcings that largely offset a substantial positive forcing from increased ozone. Moving to 2050, the models now diverge in their net values as well as the individual contributions. The GFDL model finds a positive radiative forcing due in nearly equal parts to increased black carbon and ozone. In contrast, 2050 radiative forcing in the GISS model again reflects an offset between positive forcing from ozone and negative particle forcing, with the largest contribution to the latter from reduced levels of black carbon. Both models show a partial cancellation of the black carbon forcing by an opposing forcing from organic carbon. Thus, the two models show somewhat consistent results for ozone, but differ dramatically for black carbon and sulfate particle. By 2100, the GFDL model has a large positive radiative forcing relative to 2000, due to the continued increase in black carbon as well as the decrease in sulfate.

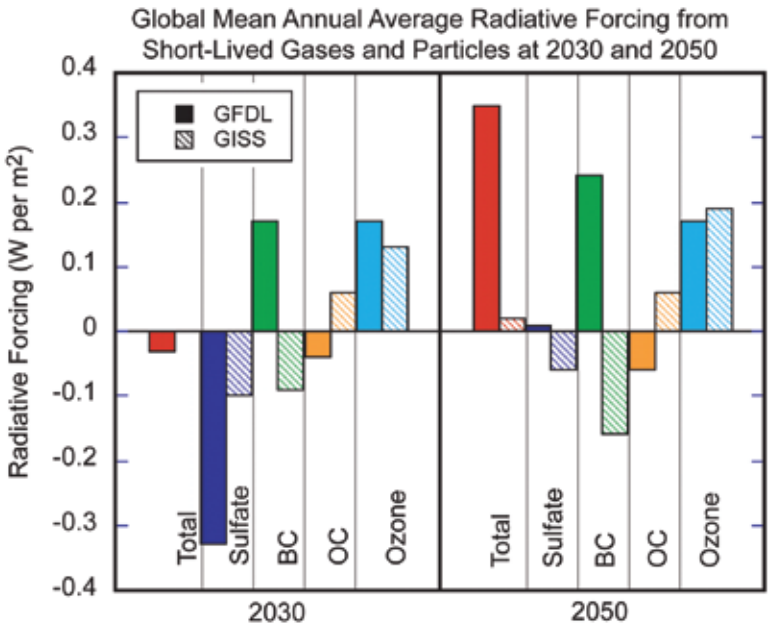

Figure 3.3 Global mean annual average radiative forcing (in W per m^2) from short-lived gases and particles at 2030 and 2050 relative to 2000. Values from the GFDL model are shown as solid bars; values from the GISS model have diagonal hatching. (Note that instantaneous forcing values from the GFDL model are shown in this figure, not the adjusted forcings shown in Table 3.6.)

Inter-model differences in radiative forcing are predominantly due to differences in modeled burdens rather than to differences in the calculation of radiative properties in the models. This can be seen clearly by examining the radiative forcing-to-burden ratio, which we term the radiative efficiency (Table 3.7). This shows fairly similar values for GFDL and GISS. The largest differences are seen for black carbon, which may reflect differences in the geographic location of projected black carbon changes as well as differing treatments of the radiative properties of black carbon. Additionally, the vertical

Table 3.6 Global mean radiative forcing for short-lived gases and particles in Watts per square meter (W per m²).

	Model	2030	2050	2100
Total	GFDL	.04	.48	1.17
	GISS	.00	.02	NA
Particles	GFDL	-.15	.24	.98
	GISS	-.13	-.17	NA
Sulfate	GFDL	-.32	.01	.51
	GISS	-.10	-.06	NA
BC	GFDL	.21	.30	.63
	GISS	-.09	-.16	NA
OC	GFDL	-.04	-.06	-.15
	GISS	.06	.06	NA
Ozone	GFDL	.19	.23	.19
	GISS	.13	.19	NA

Values are annual average radiative forcings at the tropopause (meteorological tropopause in the GISS model, "linear" tropopause in the GFDL model). "Particles" is the total of sulfate, black carbon (BC), and organic carbon (OC) (plus nitrate for GISS) particles. GISS values do not include particle indirect effects that were present in that model.

GFDL values are for adjusted radiative forcing; GISS values are for instantaneous radiative forcing (Box 3.2). The GFDL values are from Levy *et al.* (2008).

distribution of the black carbon changes will affect the radiative forcing, as will their location relative to clouds. Variations in modeling the particle uptake of water, which can have a substantial impact on the aerosol optical depth, do not seem to play a very large role in the global mean radiative forcing judging from the fairly close agreement in the two models' sulfate radiative efficiencies (Table 3.7). They may contribute to about 20 percent difference in the radiative forcing-to-burden ratios for sulfate, however. Examination of the radiative forcing-to-aerosol optical depth change (Table 3.7) shows that given a particular aerosol optical depth change, the models are in good agreement as to the resulting radiative forcing. We caution that this result contrasts with a wider model study that found larger differences in this ratio (Schulz *et al.*, 2006), though the variation in radiative forcing-to-aerosol optical depth across models was still less than the variation in aerosol optical depth itself. This suggests a possible further source of model differences that could exist were different models to be used in a study such as this.

Both the GFDL and GISS models show a positive forcing from ozone that stems partially from increased tropospheric ozone concentrations (Table 3.2) due to increased NO_x emissions (Table 3.1) and partially from the recovery of stratospheric ozone due to reductions in emis-

Table 3.7 Radiative efficiency.

Species	Model	(W per m²)/ Tg	(W per m²)/ AOD
BC	GFDL	2.8	104
	GISS	1.5	94
OC	GFDL	-.18	NA
	GISS	-.16	NA
Sulfate	GFDL	-.47	-16
	GISS	-.59	-16

Values are given for the radiative efficiency in terms of the radiative forcing-to-burden ratio and the radiative forcing-to-aerosol optical depth (AOD) ratio. All values are global-mean, annual-mean averages. Values for radiative forcing and burden or aerosol optical depth changes are for 2050 versus 2000 for black carbon (BC) and organic carbon (OC), and 2030 versus 2000 for sulfate in order to analyze the largest changes for each particle. GISS values for the sulfate burden changes include only the portion of sulfate not absorbed onto dust, as this portion alone is radiatively important.

sions of ozone-depleting substances (primarily halogens). The forcing from the tropospheric portion of the ozone changes is substantially more important, however (Shindell *et al.*, 2007). (The NCAR group did not calculate the radiative forcing, but forcing in their model is likely to have been similar, as they found an increase in the tropospheric ozone burden from 2000 to 2050 of 15.0 Dobson Units [DU], very close to the GISS value of 16.2 DU [Table 3.2].) As shown previously, however, the apparent sensitivity of ozone burden to changes in NO_x emissions differs substantially between the GISS and GFDL models. Thus the similarity in the radiative forcing may be largely fortuitous, resulting from a cancellation of changes in emissions and of sensitivities of ozone to NO_x emissions.

Increases in low-level ozone provide much more potential for future warming than the increase in upper-level ozone.

Thus, at 2030, differences in the physical processes in the two models dominate the differences in radiative forcing between the two models. The large divergence in radiative forcing from sulfate stems from both the chemical conversion efficiency of SO_2 to sulfate being more than a factor of two larger in the GFDL model than in the GISS model, and the greater role of sulfate in producing aerosol optical depth in the GFDL model. In addition, the GISS model includes a substantial absorption of sulfate onto dust, a process that is highly uncertain. Such a process would reduce the radiative forcing due to sulfate. At 2050, emissions and concentrations of sulfur dioxide have returned to near their 2000 level, so that these differences are not so important at this time. Hence, the 2050 differences between the two models are dominated by differences in black carbon emissions projections and not by differences in physical processes. Differences in the residence times and radiative efficiencies for black carbon are substantial but tend to offset.

On a hemispheric scale, the GISS and GFDL models again differ greatly (Table 3.8). The GFDL model shows a very large positive forcing in the Northern Hemisphere in 2050 due primarily to reductions in emissions of sulfate precursors and increased emissions of black carbon. Increases in sulfate precursor emissions from developing countries lead to a negative forcing in the Southern Hemisphere in the GFDL model. In the GISS model, the sign of the total net forcings are reversed, with negative values in the Northern Hemisphere and positive in the Southern Hemisphere (Table 3.8). The GISS results are primarily due to the reduction in BC in the Northern Hemisphere and the influence of increased ozone and reduced OC in the Southern Hemisphere (where sea salt dominates the aerosol optical depth, so that anthropogenic particle emissions changes are relatively less important).

3.3.3.2 Regional Forcing Patterns

The differences in hemispheric and global forcings can be attributed to strong forcing changes in particular regions, and hence to regional emissions as the radiative forcing is typically localized relatively close to the region of emissions. Comparison of the spatial patterns of radiative forcing in the GISS and GFDL models reveals that the starkest discrepancies occur in the developing nations of South and East Asia (Figure 3.4). The emissions scenario used by the GISS model projects strong increases in SO_2 emissions from India, with little change over China. In contrast, the scenario used by the GFDL model has large decreases in sulfate emissions in both regions, especially China.

Table 3.8 Hemispheric radiative forcing (W per m²).

	Model	2030	2050	2100
Northern Hemisphere	GFDL	.15	1.09	1.91
	GISS	-.15	-.14	NA
Southern Hemisphere	GFDL	-.09	-.14	.42
	GISS	.16	.18	NA

Values are the net annual average forcings at the tropopause in each hemisphere from particles and ozone. GISS forcing values do not include particle indirect effects that were present in that model.

The scenarios are much more similar for the developed world, with both projecting reductions in sulfate precursor emissions for North America and Europe, for example, leading to a positive radiative forcing in both cases. Differences between the scenarios are even larger for black carbon, which increases throughout most of the Northern Hemisphere in the GFDL model but decreases in the

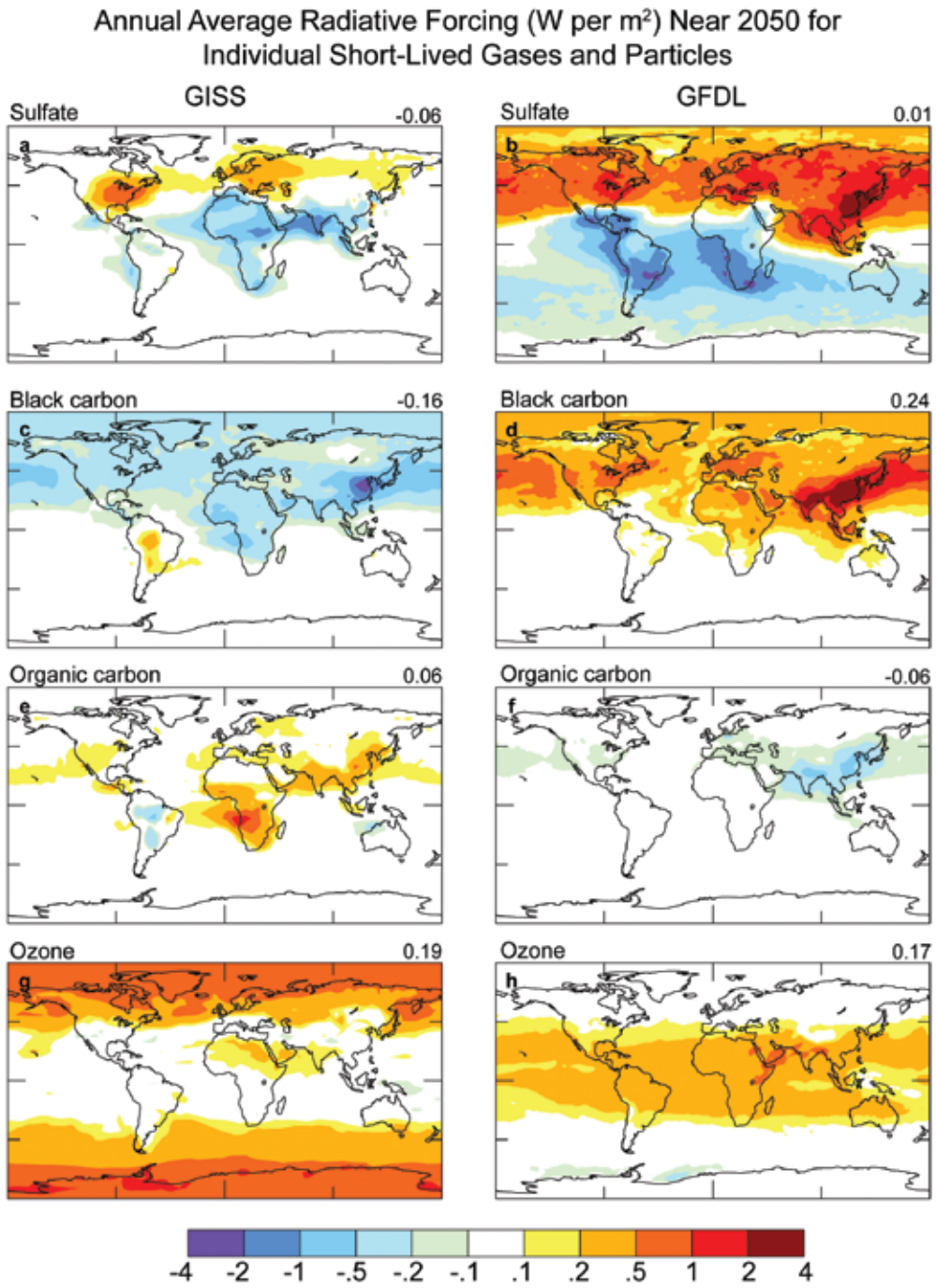

Figure 3.4 Annual average instantaneous radiative forcing (W per m²) near 2050 relative to 2000 for the indicated individual short-lived gases and particles in the GISS (left) and GFDL (right) models. Radiative forcing from long-lived gases is largely spatially uniform over the globe. (Note that the instantaneous forcings shown here for the GFDL model differ from the adjusted forcings shown in Table 3.6.)

GISS model. Again, however, the divergence is especially large over South and East Asia, where the GISS model has large reductions while the GFDL model has large increases (Figure 3.4). Thus the differences in the global total emissions discussed previously (Figure 3.1; Table 3.1) and in the global radiative forcing (Figure 3.2; Table 3.6) arise primarily from differences in projected emissions from developing countries in Asia.

The radiative forcing from organic carbon is generally similar in its spatial pattern to black carbon, but of opposite sign and substantially reduced magnitude (25 to 40 percent of the black carbon radiative forcing). Substantial

The differences in the global total emissions arise primarily from differences in projected emissions from developing countries in Asia.

differences again occur between the emissions scenarios of the two models, this time primarily over African biomass burning regions. As discussed previously, the GFDL model assumed that biomass burning emissions would scale with one-half the factor used for purely anthropogenic emissions, while the GISS model instead used regional biomass burning emissions projections (Streets *et al.*, 2004), with substantial reductions in African biomass burning.

The spatial pattern of radiative forcing from ozone is also very different in the two models (Figure 3.4). However, this forcing is not so closely tied to the region of precursor emissions in the GISS model where much of the forcing is related to an increased flux of ozone into the troposphere owing to the recovery of lower stratospheric ozone. This leads to substantial positive forcing in that model at high latitudes, even without including the effects of climate change on circulation (Section 3.3.3.4). At low latitudes, GISS shows little forcing as the modeled increase in upper stratospheric ozone causes negative radiative forcing, offsetting some of the forcing from tropospheric ozone increases, and alters lower level photochemistry. Furthermore, the particle indirect effect in that model influences cloud cover and wet deposition, which seems to reduce tropospheric ozone at low latitudes in comparison with simulations not including the particle indirect effect. The GFDL model does not show a similar high latitude enhancement, however, but instead shows maximum ozone forcing in the tropics. This may reflect a greater geographic shift in emissions to lower latitudes, a greater efficiency in transporting ozone and its precursors to the upper troposphere, where ozone has the greatest positive forcing efficiency, and differences in the relative importance of change in the overlying stratospheric ozone column. The GFDL radiative forcing is similar to results from models with tropospheric ozone only and no particle indirect effects (Gauss *et al.*, 2003).

3.3.3.3 Effects of Uncertainties in Methane Concentrations on Radiative Forcing

The SAP 3.2 simulations included methane concentrations prescribed to A1B values from the AIM integrated assessment model, for consistency with the long-lived gas runs. To investigate the potential uncertainty in the methane value derived by that integrated assessment model, the GISS model performed an additional 2050 simulation using its internal methane cycle model (Shindell *et al.*, 2007). The simulation included prescribed anthropogenic emissions increases from the AIM model to allow comparisons with the AIM results used in the results in this chapter. Natural spatially and seasonally varying emissions and soil adsorption were the standard amounts described in Shindell *et al.* (2003). Both the methane emissions from wetlands and the biogenic isoprene emissions were interactive with the climate in this run (Guenther *et al.*, 1995; Shindell *et al.*, 2004), though the distribution of vegetation did not respond to climate change.

Methane's oxidation rate is calculated by the model's chemistry scheme in both the troposphere and stratosphere. Thus methane can affect its own lifetime (which is primarily governed by tropospheric oxidation rates), as can other molecules that compete with methane for hydroxyl radicals (the main oxidizing agent), such as isoprene. The simulations included 2050 surface climate (sea surface temperatures and sea ice, taken from an earlier climate model run). Changes in water vapor induced by the altered climate affect methane oxidation in those runs. Methane was initialized with estimated 2050 abundances and the simulations were run for three years. We note that the IMAGE integrated assessment model projected a continuous increase in methane emissions; this is rather different from the increase through 2030 and slow decrease thereafter in the AIM integrated as-

sessment model. At 2050, for example, this led to projected anthropogenic methane emissions of 512 Tg C per year in the IMAGE model, substantially greater than the 452 Tg C per year from the AIM model used here (compared with 323 Tg C per year for 2000).

We find that methane emissions from wetlands increase from 195 to 241 Tg C per year while emissions of isoprene increase from 356 to 555 Tg C per year. Additionally, even in the absence of changes in emissions from natural sources, the projected anthropogenic emissions of ozone precursors (including methane itself) increase the lifetime of methane while climate change reduces it via increased temperature and water vapor (Table 3.9). These responses to anthropogenic emissions and to climate change without interactive emissions are qualitatively consistent with those reported from a range of models (using different emissions projections) in Stevenson *et al.* (2006). The effect of precursor emissions is stronger in our scenario, so that the net effect of anthropogenic emissions and climate changes is to increase methane's lifetime. When natural emissions are also allowed to respond to climate change, increased competition from isoprene and increased methane emissions from wetlands lead to further increases in methane's lifetime (Table 3.9) and enhanced methane abundance.

The 2050 simulation with the model's internal methane cycle had a global mean surface methane value of 2.86 ppmv in year three, with sources exceeding sinks by 80 Tg C per year (a growth rate that may reflect an overestimate of the loss rate in the AIM model used in the initial guess). Extrapolating the change in methane out to equilibrium using an exponential fit to the three years of model results yields a 2050 value of 3.21 ppmv.

We have calculated radiative forcings using the standard calculation (Table 6.2 in Ramaswamy *et al.*, 2001) assuming an increase in N_2O from 316 to 350 ppb in 2050, following the A1B "marker" scenario (using the AIM integrated assessment model). The 2050 methane forcing using the methane concentration specified in the A1B "marker" scenario would be 0.22 W per m^2 while using the larger methane concentrations of 2.86 or 3.21 ppmv calculated with our model gives 0.36 or 0.46 W per m^2, respectively. Of course, it is difficult to estimate methane's abundance at a particular time without performing a full transient methane simulation. However, uncertainty in the forcing from methane appears to be at least 0.1 to 0.2 W per m^2. Note that use of the 40 percent larger anthropogenic methane emissions increase from the IMAGE integrated assessment model would have led to a substantially larger forcing. Should the results of our modeling of the methane cycle prove to be robust, this would imply that future positive forcing from methane might be substantially larger than current estimates based on integrated assessment model projections.

We note that while the A1B projections assume a substantial increase in atmospheric methane in the future, the growth rate of methane has in fact decreased markedly since the early 1990s and leveled off since ~1999 (Dlugokencky *et al.*, 2003). Hence, the projections may overestimate future atmospheric concentrations. However, there are indications that the growth rate decrease was primarily due to reduced anthropogenic emissions, and that these have been increasing again since 1999 (though masked by a coincident decrease in natural methane emissions) (Bousquet *et al.*, 2006). All of this suggests that atmospheric methane may in fact increase substantially again in the future, as assumed by the integrated assessment models, although other methane studies have argued for an increase in its principal loss path as the explanation, rather than changes in emissions (*e.g.*, Fiore *et al.*, 2006). Other emissions, such as NO_x from lightning and from soil and dimethyl-sulfide from the oceans, are also expected to respond to climate change. Changes in land

There is considerable uncertainty in methane-driven climate changes in future scenarios. They could be larger than currently anticipated.

Table 3.9 Methane lifetime in GISS simulations. Includes calculated photochemical loss (in troposphere and stratosphere) and prescribed 30 Tg C per year loss to soils.

Run	Lifetime (years)
2000	9.01
2030	9.96
2050	10.39
2030 with climate change	9.72
2050 with climate change	10.01
2050 with methane cycle	10.42

cover would also affect both emissions and removal of trace gases and particles. Further work is required to gauge the importance of these and other climate-chemistry feedbacks.

3.3.3.4 Effects of Climate Change on Radiative Forcing

The chemical composition simulations (Section 3.2) did not include the effects of climate change on the short-lived gases and particles, only the effects of projected changes in anthropogenic emissions. Separate sets of simulations with the GISS model included climate change via prescribed sea-surface temperatures and sea-ice cover taken from prior runs. Climate change increased the radiative forcing from ozone by increasing stratosphere-troposphere exchange (STE) and hence ozone near the tropopause where it is most important radiatively (Hansen *et al.*, 1997). This effect outweighed increased reaction of excited atomic oxygen with the enhanced tropospheric water vapor found in a warmer climate, which led to ozone reductions in the tropical lower troposphere. The overall impact was to increase radiative forcing by .07 W per m^2 in 2050. Climate change slightly increased the negative forcing from sulfate (by .01 W per m^2), consistent with an increase in tropospheric ozone in these runs (as ozone aids in sulfur dioxide oxidation both directly and via hydroxyl formation).

There may be significant feedbacks of climate change on ozone concentration and dust emissions.

Dust emissions decreased slightly (about five percent at 2050) in these climate runs, but there was more sulfate on dust, suggesting that this played only a minor role in the sulfate forcing response to climate change. The reduction in dust would itself lead to a slight negative forcing (approximately 0.02 W per m^2). However, emissions in the model respond only to changes in surface wind speeds, and not to changes in sources due to either CO_2 fertilization or climate-induced vegetation changes which have a very uncertain effect on future dust emissions (Mahowald and Luo, 2003; Woodward *et al.*, 2005).

Much of the increase in ozone forcing results from an increase in stratosphere-troposphere exchange in the GISS model of 134 Tg per year (about 20 percent of its present-day value) as climate warms. An increase in transport rates between the stratosphere and the troposphere is a robust projection of climate models (Butchart *et al.*, 2006). Combined with the expected recovery of stratospheric ozone, this should enhance the influx of stratospheric ozone into the lower atmosphere. However, the net effect of climate change on ozone is more difficult to determine as it results from the difference between enhanced stratosphere-troposphere exchange and enhanced chemical loss in the troposphere in a more humid environment, which is not consistent among climate models (Stevenson *et al.*, 2006).

3.3.4 Climate Model Simulations 2000 to 2050

As discussed in Section 3.3.1, the experimental design consists of two sets of simulations: (1) the effects of changes in short-lived and long-lived gases and particles in the twenty-first century (employing the A1B scenario for the evolution of the long-lived gases and the output from the composition models discussed in Section 3.2 for the short-lived gases and particles); (2) the effects of changes in the long-lived gases only, with the short-lived gases and particles concentrations held at 2000 values. The effects of short-lived gas and particle changes are determined by subtracting the climate responses of the runs with changes in long-lived gases only from those with changes in long-lived and short-lived gases and particles. This procedure is justified by studies showing that the climate response to changes in radiatively active species is generally linear (Ramaswamy and Chen, 1997; Haywood *et al.*, 1997; Cox *et al.*, 1995). Simulations where only the short-lived gases and particles change were not included in the experimental design, because such scenarios are neither realistic nor policy relevant.

3.3.4.1 Surface Temperature Changes

The global-mean annual-mean surface temperature responses to short-lived gases and particles in the three different models are not as dissimilar as one might have expected, given the different emissions used and the different physical processes included. The CCSM model ran only a single simulation, which showed little or no statistically significant[5] effects of the short-lived gases and particles on global mean surface temperatures. The GFDL and

[5] The statistical methods used to assess significance are discussed in Box 3.3.

BOX 3.3: Statistical Methods

A result is deemed to be statistically significant if it is unlikely to have occurred by chance (*i.e.*, the probability that it occurred by chance is less than some specified threshold). A 95 percent confidence level means that the odds are 20:1 against the result having occurred by chance.

Statistical significance in the GFDL climate model results was evaluated using two approaches. For global-mean, or hemispheric-mean results involving a temperature departure from the initial (2000) value, the range (highest to lowest temperature change) of the three ensemble members used to obtain the ensemble-mean result was computed. The ensemble-mean result was deemed significant if that range was entirely different from zero. For regional (latitude-longitude) results comprising the difference of two time series, as in the evolution of temperature change due to short-lived species, the Student's-*t* test for significance was applied at each model grid point, with the result deemed significant if the statistical test showed significance at the 95 percent confidence level.

GISS models both ran three-member ensemble simulations, and both show a statistically significant[5] warming effect from short-lived gases and particles from around 2030 to the end of the runs (Figure 3.5). The GFDL model shows a warming of 0.28°C (ensemble mean 2046 to 2050). This value is commensurate with the adjusted radiative forcing of about 0.48 W per m^2 computed for 2050. The GISS model shows substantially more warming (approximately 0.13°C near 2050) than would be expected from the direct radiative forcing in that model and its climate sensitivity (λ = approximately 0.6°C [W per m^2 per year]) owing to the presence of the particle indirect effect, which contributes additional warming as particle loading decreases in the future (Shindell *et al.*, 2007).

Changing levels of short-lived gases and particles contribute approximately 20 percent of the overall global annual average warming in these two models (17 percent for GISS and 27 percent for GFDL based on 2046 to 2050 *vs.* the first five years of the run). It is important to note, however, that these models respond as they do for different reasons.

In the GFDL simulations, reduced sulfate and increased black carbon and ozone all combine to cause warming. In contrast, in the GISS model, the warming results from increased ozone and a reduced particle indirect effect, with a substantial offset (cooling) from reduced black carbon. The lack of a substantial effect from short-lived gases and particles in the CCSM simulations is attributable to the emissions used, which produce small increases in sulfate (cooling) and small increases in black carbon (warming) that largely offset one another (thus their radiative forcing changes little from 2000 to 2050).

Hemispheric temperatures show trends largely consistent with the radiative forcings (Table 3.8), namely substantial warming in the Northern Hemisphere in the GFDL model and in the Southern Hemisphere in the GISS model (Figure 3.6). The Northern Hemisphere warming in the GFDL model is driven primarily by the large decreases projected for sulfate and the large increase projected for black carbon in that model for the industrialized areas of the

Two of the three models show substantially increased global warming as a result of changes in short-lived gases and particles.

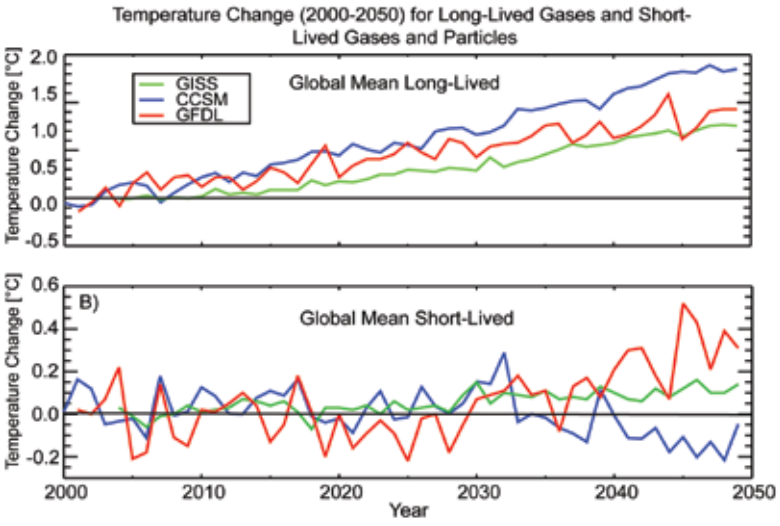

Figure 3.5 Global mean annual average temperature change (°C) in the simulations with time-varying long-lived (top) and short-lived (bottom) gases and aerosols. Results are three-member ensemble means for GFDL and GISS and single-member simulations for CCSM. Results for the short-lived gases and aerosols are obtained by subtraction of the (long-lived) calculations from the (short + long-lived) calculations.

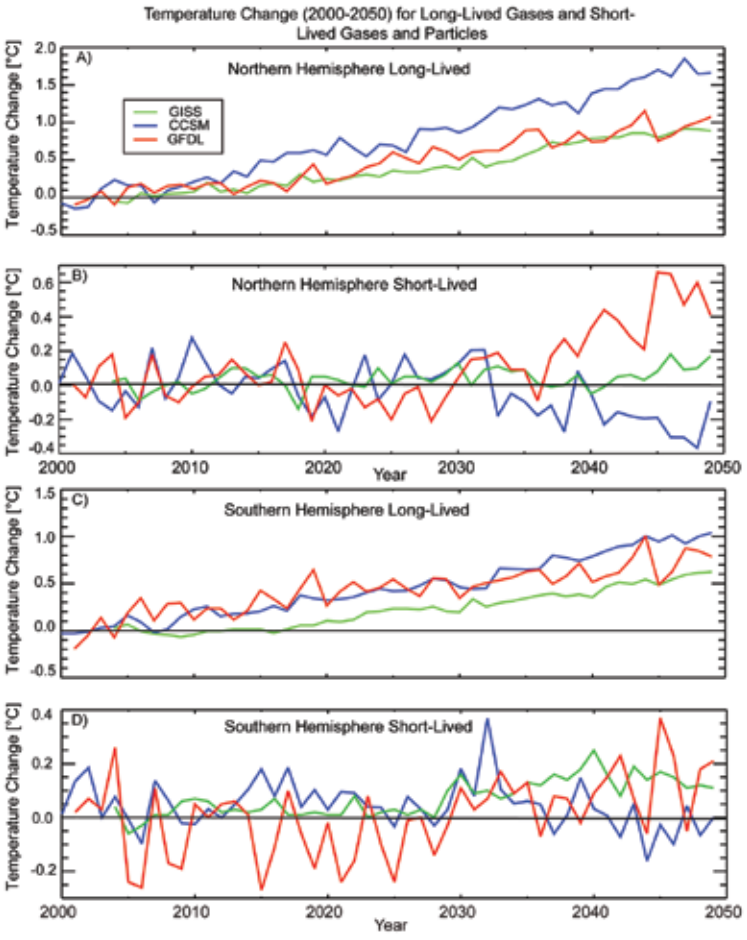

Figure 3.6 Hemispheric mean annual average temperature change (°C) in the simulations with time-varying long-lived and short-lived gases and particles. All the results are three-member ensemble means for GFDL and GISS and single member simulations for CCSM. Results for the short-lived gases and particles are obtained by subtraction of the (long-lived) calculations from the (short+long-lived) calculations.

Northern Hemisphere (Levy *et al.*, 2008). This causes the aerosol optical depth from sulfate to drop by one-third in the Northern Hemisphere by 2050 while the aerosol optical depth from black carbon increases by 50 percent. The large change in sulfate dominates the overall aerosol optical depth change in that model (Table 3.5). The magnitude of the Northern Hemisphere warming is ~0.5°C by 2050, consistent with the ~1.1 W per m^2 radiative forcing in that model, when one accounts for the fact that the warming has not been fully realized due to the lag-time for oceanic heat adjustment (Stouffer, 2006). There is an overall negative forcing in the Southern Hemisphere in the GFDL model, as sulfate precursor emissions increase in the developing world while black carbon changes little. Some of the negative forcing from particles in the Southern Hemisphere is offset by positive forcing from ozone, which increases rather uniformly over much of the world in that model (Levy *et al.*, 2008), leading to a small net effect and minimal temperature change from short-lived gases and particles (Figure 3.6).

The change in the forcing due to the particle indirect effect in the GISS model was argued to be on the order of 0.1 W per m^2 in 2050 (Shindell *et al.*, 2007). Combining this with the GISS hemispheric radiative forcings (excluding the indirect effect) in Table 3.8 yields a Northern Hemisphere radiative forcing near zero and a Southern Hemisphere forcing of about 0.3 W per m^2. These forcings are consistent with the warming of about 0.15°C seen in that model in the Southern Hemisphere and the lack of response in the Northern Hemisphere. Northern Hemisphere aerosol optical depth changes are dominated by a substantial reduction in black and organic carbon (the black carbon aerosol optical depth in the Northern Hemisphere falls by nearly 50 percent), which more than offsets a slight increase in sulfate (particularly as this model is less sensitive to sulfate). These particle changes lead to negative Northern Hemisphere forcing. In the Southern Hemisphere, the GISS model shows only small changes in particles, so that positive forcing from ozone dominates the net radiative forcing. The particle indirect effect further accentuates the positive forcing owing to reductions in black carbon and organic carbon. The signs of the temperature response in the two hemispheres are thus opposite in the GISS model to what they are in the GFDL model.

As for the global case, trends in the CCSM model are not significantly different in the runs with and without short-lived gases and particles. This is the result of only a miniscule change in aerosol optical depth in the Northern Hemisphere (-2 percent), as sulfate and carbonaceous particle precursor emissions are both near their present-day values by 2050 in that model. In the Southern Hemisphere, there is an increase in aerosol optical depth from 2000 to 2050, which seems to be primarily due to sulfate, but this is largely offset by increased ozone in the Southern Hemisphere as stratospheric ozone recovers.

Thus it is clear that at global and especially at hemispheric scales, the three climate models are being driven by substantially different trends in their short-lived gases and particles. These differences in particles are largely related to the differences in the projected emissions of particle precursors, though there is some contribution from differences in particle modeling as discussed previously. Additionally, the climate response of each model is different to some extent owing to the inclusion of different physical processes in the models, especially the inclusion of the particle indirect effect in the GISS model. However, the above analysis strongly suggests that the largest contributor to the inter-model variations in projected warming arise from different assumptions about emissions trends.

At smaller spatial scales, the annual average patterns of surface temperature changes induced by the short-lived gases and particles show even larger divergences (Figure 3.7). Around 2030, the largest responses are seen at Northern middle and high latitudes. These show large regions of both cooling and warming that are characteristic of the response to changes in atmospheric circulation. Most of the response at middle and high latitudes is not statistically significant in the models owing to large natural variability. Surprisingly, all three models show similar patterns of cooling near Alaska and a region of warming over Siberia. Other regions, such as the Labrador Sea/Baffin Island area or Scandinavia, show substantial variations between models, again suggesting these middle and high latitude dynamic responses are not robust.

In the tropics, where dynamic variability is much smaller, the models find much greater areas with statistically significant responses, especially by 2050. The CCSM model finds a small but significant cooling over tropical oceans, while the other models find warming.

It is clear that especially at hemispheric scales, the three climate models are being driven by substantially different trends in short-lived gases and particles.

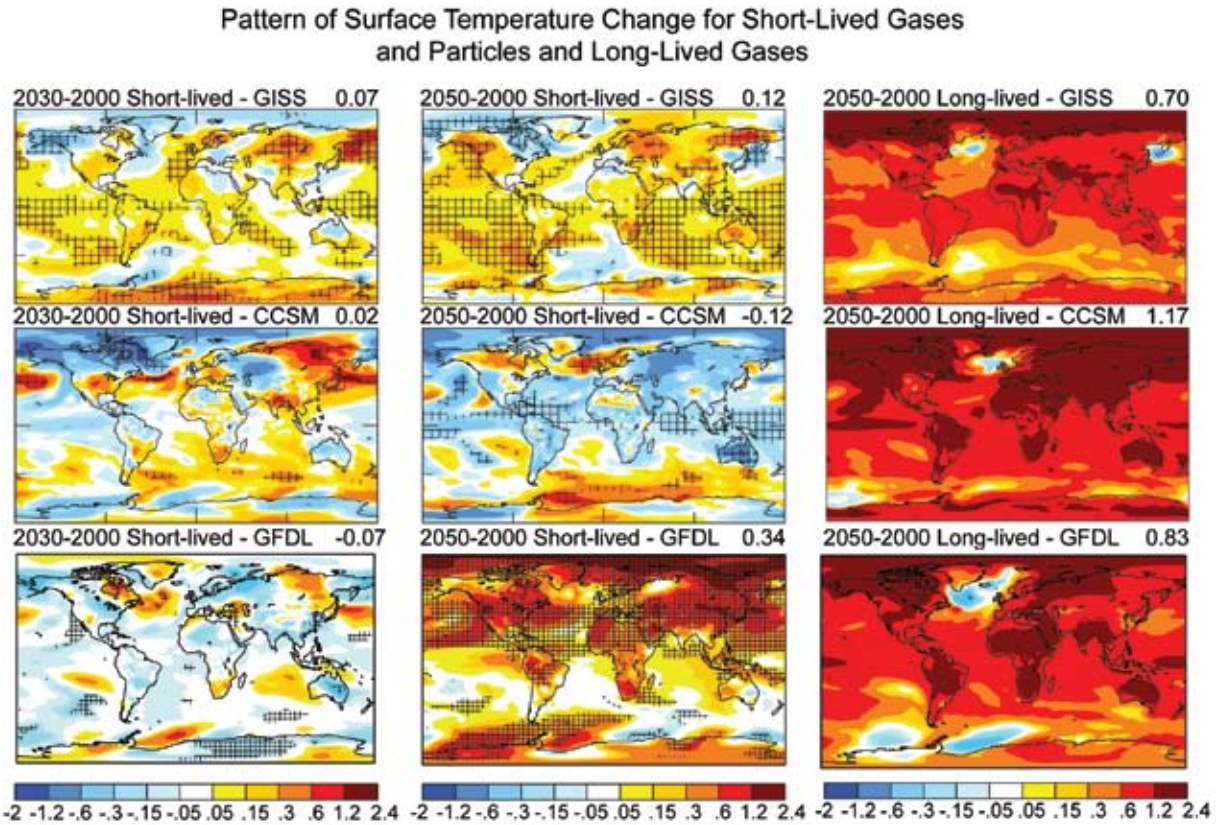

Figure 3.7 Annual average surface temperature response (°C) in the climate models to short-lived gases and particles (left and center columns) and long-lived gases (right column) changes for the indicated times. The changes at 2030 are 2020 to 2029 in the CCSM and GFDL models and 2028 to 2033 in the GISS model. At 2050, they are 2040 to 2049 in the CCSM model, 2046 to 2055 in the GFDL model, and 2040 to 2050 in the GISS model. Hatching indicates statistical significance (95 percent) for the response to short-lived gases and particles. All colored values above 0.1°C are statistically significant in the response to long-lived gases. Values in the upper right corners give the global mean.

As in the global-mean case, this appears to arise from differences in particle burdens and aerosol optical depths.

In the Arctic, the GISS and CCSM models find primarily a cooling effect from projected changes in short-lived gases and particles (especially near 2030 for GISS, and 2050 for CCSM). In contrast, the GFDL model finds a substantial warming there. This may be due in part to the increasing trend in black carbon in that model.

The United States and other Northern Hemisphere industrialized regions might be especially sensitive due to the projected reduction in sulfate precursor emissions in the Northern Hemisphere.

In the Antarctic, the GISS model shows warming related primarily to stratospheric ozone recovery. The GFDL model shows a similar result by 2050 (after which stratospheric ozone was unchanged in that model). CCSM does not show as clear an Antarctic warming, however, even though this model also included recovery of ozone in the Antarctic lower stratosphere. This is surprising given that the CCSM model appeared to show a substantial response to ozone depletion in analyses of the Southern Hemisphere circulation in IPCC AR4 simulations (Miller *et al.*, 2006b). That analysis showed that most climate models found a general strengthening of the westerly flow in the Southern Hemisphere in response to stratospheric ozone depletion. A stronger flow isolates the polar region from lower latitude air, leading to cooling over the Antarctic interior and warming at the peninsula. Conversely, recovery should lead to warming of the interior (enhanced by the direct positive radiative forcing from increased ozone), as in the GISS and GFDL simulations. However, in the GISS model the effect diminishes with time, suggesting that other aspects of the response to short-lived gases and particles become more important in these scenarios over time, presumably as projected particle changes grow ever larger.

Warming over the central United States is present in the GISS model at all times (but is not statistically significant), in the GFDL model from about the 2040s on, and in the CCSM model around 2030, but not at 2050. The United States and other Northern Hemisphere industrialized regions might be especially sensitive to the projected reduction in sulfate precursor emissions in the Northern Hemisphere. This effect is especially large in the GFDL model, where forcings from sulfate decreases and black carbon increases both contribute to warming, though it should be noted that the largest radiative forcing is over Asia, not over the United States and Europe (Figure 3.4). In the CCSM model, the warming effect vanishes by 2050 as both sulfate and black carbon decrease, producing temperature responses that cancel. In the GISS model, reductions in sulfate and increases in ozone both contribute to warming; however, these are partially offset by cooling from reduced black carbon.

The surface temperature changes induced by the long-lived gases are clearly much larger than those induced by short-lived gases and particles over most of the Earth by 2050 (Figure 3.7). In some regions, however, the two are of comparable magnitude (*e.g.*, the polar regions and parts of the Northern midlatitude continents in the GFDL model, parts of the Southern Ocean in the GISS model) though the statistical significance of the signal for short-lived gases and particles is marginal. Consistency between the models is also clearly greater in their response to long-lived than to short-lived gases and particles.

Overall, it is clear that the regional surface temperature response does not closely follow the regional radiative forcing patterns based on either GISS or GFDL results. Both models show very large forcings over East Asia, for example, yet have minimal response there. This is especially clear when comparing the seasonal radiative forcings and climate response (Figure 3.8). Though some of the spatial mismatches could result from a lag in the climate response

to seasonally varying forcings, the divergence between the patterns of forcing and response is large even for areas with minimal seasonality in the forcing (*e.g.*, Africa, subtropical Asia). See Section 9.2.2.1 of Chapter 9 in the Fourth IPCC assessment (Hegerl *et al.*, 2007) and references therein for further discussion of this issue.

3.3.4.2 Precipitation, Sea-Level, and Other Variables.

Changes in other climate variables (such as precipitation and sea level) due to short-lived gases and particles are typically too small to isolate statistically. In the case of precipitation, this is due to the high variability of the precipitation signal. The relatively short (50 year) length of the integrations discussed here accounts for the lack of a significant sea-level signal. Sea level is expected to rise in a warming climate, chiefly due to thermal expansion of the oceans. In the GISS and GFDL models, the thermal expansion would be enhanced by about 20 to 25 percent due to changes in short-lived gases and particles. Similarly, the enhancement of precipitation along the equator and drying of the subtropics that is a robust feature of climate models in a warming climate (Held and Soden, 2006) would also be accentuated in the GFDL and GISS models with their significant tropical warming, though probably not under the CCSM scenario. Such a feature can indeed be seen in the GISS response in the Atlantic and Indian Oceans.

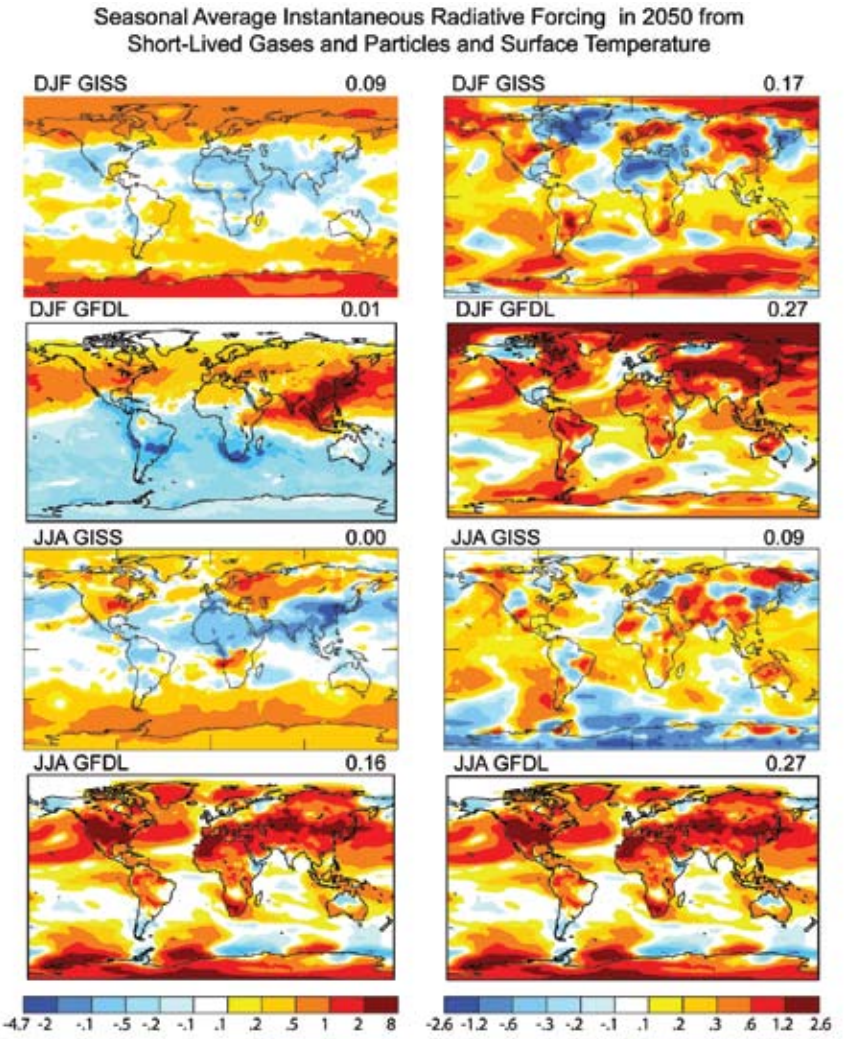

Figure 3.8 Seasonal average instantaneous radiative forcing (W per m^2) in 2050 from short-lived gases and particles (left column) and surface temperature response in °C (right column) in the GISS and GFDL models. Boreal winter (December through February) is shown in the top two rows, while boreal summer (June through August) is shown in the bottom two rows. The temperature changes at 2050 are 2046 to 2055 in the GFDL model and 2041 to 2050 in the GISS model. Values in the upper right corners give the global mean. (Note that the instantaneous forcings shown here for the GFDL model differ from the adjusted forcings show in Table 3.6.)

On a regional scale, there are some suggestions of precipitation trends but statistical significance is marginal for either annual or seasonal changes. The CCSM model shows reductions in winter precipitation due to short-lived gases and particles across most of the United States in the 2040s, and reductions in summer precipitation in the southeastern part of the United States. That model also suggests an increase in summer monsoon rainfall over South Asia. In contrast, the GISS model shows slight increases in winter precipitation over the central United States, and a mixed signal in summer (and spring) with increased precipitation over the Southeast and Southwest United States, but decreases over the Northeast United States. During fall, precipitation decreases over most of the country. As in the CCSM model, there is an increase in summer (and fall) precipitation over South Asia. In the annual average, the GFDL model shows no statistically significant trend over the United States. Given that significant trends are hard to identify in any of the models, and that the models do not agree on the trends themselves, we believe that it is not possible to reliably estimate precipitation trends owing to short-lived gas and particle changes under the A1B storyline.

The surface temperature changes induced by the long-lived gases are clearly much larger than those induced by short-lived gases and particles over most of the Earth by 2050 (Figure 3.7). In some regions, however, the two are of comparable magnitude.

3.3.4.3 Discussion

In the transient climate simulations, three climate models examined the response to projected changes in short-lived gases and particles. The results shown in Figure 3.7 differ substantially among the models, particularly by 2050. Comparison has shown that the differences in the underlying emissions projections are the dominant source of inter-model variations in projected particle trends. These variations result from differences between the various integrated assessment models that provided those projections and to assumptions made about emissions not provided by the integrated assessment models.

Uncertainties in the representation of radiative processes are an additional source of differences in the temperature response of the three models. For example, the GFDL model's aerosol optical depth is substantially more sensitive to sulfate than the GISS model, with the CCSM model in between. This is partially due to the inclusion of sulfate absorption onto dust being present only in the GISS model. Additionally, the indirect effect of particles is included only in the GISS model. Thus, the inclusion of different physical processes plays a role in the inter-model differences, and is especially important near 2030, when sulfur dioxide (SO_2) emissions are near their peak. With the inclusion of the particle indirect effect, the GFDL model might yield a substantially larger warming, given that sulfate is the largest contributor to particle mass globally and that the GFDL sulfate concentrations decrease beyond 2030.

Differences in the models' representation of the hydrologic cycle, which removes soluble gases and particles, and in oxidation may also produce variations in the temperature response. Inter-model differences between the GFDL and GISS models in the residence times of particles are substantial for sulfate, and differences in the radiative effect of black carbon are also potentially sizeable. In nearly all cases, however, these are outweighed by emissions differences. Exceptions are sulfate in 2030 and tropospheric ozone; differences in the modeled conversion of SO_2 to sulfate and the sensitivity of ozone to NO_x emissions are larger than differences in projected precursor emissions. Hence, in these cases uncertainties in physical processes, including chemistry, dominate over uncertainties in emissions. These differences between GFDL and GISS model results appear to be representative of other intermodel differences, such as those identified for modeling of sulfate and black carbon particles in recent comparisons between a large suite of models (Schulz *et al.*, 2006).

We also reiterate that uncertainties in the particle indirect effect and in internal mixing between particle types are either not included at all or only partially in these simulations. Sensitivity studies and analysis of the GISS model results indicates that the forcing from reductions in the particle indirect effect is roughly 0.1 to 0.2 W per m^2, while the inclusion of sulfate absorption onto dust reduces the negative forcing from sulfate at 2030 or 2050 by up to 0.2 W per m^2 (Shindell *et al.*, 2007), These sensitivities suggest that uncertainties in these processes could alter the global mean projected temperature trends by up to 0.1°C at 2030 or 2050, a value comparable to the total temperature trend in that model. Hence without the particle indirect effect, the GISS model would likely have shown minimal warming, while without sulfate absorption onto dust surfaces, it would likely have shown a substantially greater warming trend (at least at 2030).

The responses of methane (and other hydrocarbon) emissions and of stratosphere-troposphere exchange to climate change can also potentially have significant impacts on radiative forcing, and these processes were not included in these simulations. As discussed in sections 3.3.3.3 and 3.3.3.4, the resulting changes to radiative forcing could again substantially alter the projected temperature trends. Additionally, given the large influence of uncertainties in emissions projections, we stress that the magnitude and even the sign of the effects of short-lived gases and particles on climate might be different were alternative emissions projections used in these same models. Thus, the response of short-lived gases and particles and methane to emissions changes and climate changes has been only partially characterized by the present study, and substantial work remains to reduce uncertainties and further clarify their potential role in future climate change.

The results clearly indicate that the spatial distribution of radiative forcing is generally less important than the spatial distribution of climate response in predicting climate impact. Thus, both short-lived and long-lived gases and particles appear to cause enhanced climate responses in the same regions of high sensitivity rather than short-lived gases and particles having an enhanced effect primarily in or near polluted areas. This result is supported by analysis of the response to larger radiative perturbations in these models for the future (Levy *et al.*, 2008) and the past (Shindell *et al.*, 2007). It is also consistent with earlier modeling studies examining the response to different inhomogeneous forcings than those investigated here (Mitchell *et al.*, 1995; Boer and Yu, 2003; Berntsen *et al.*, 2005; Hansen *et al.*, 2005). This suggests that the mismatch between model simulations of the regional patterns of twentieth century climate trends and observations is likely not attributable to unrealistic spatially inhomogeneous forcings imposed in those models. Instead, the models may exhibit regional climate sensitivities that do not match the real world, and/or some of the observed regional changes may have been unforced (*i.e.*, the result of internal variability [see Knutson *et al.*, 2006 for a discussion of this issue]).

3.3.5 Climate Simulations Extended to 2100

Following the A1B "marker" scenario into the second half of the 21st century for both three-member ensembles, the GFDL simulations (Levy *et al.*, 2008) find significant climate impacts due to emissions of sulfur dioxide (SO_2), the precursor of sulfate particle, (which decrease to ~35 percent of 2000 levels by year 2100) and of black carbon (scaled to carbon monoxide emissions in the GFDL model) which continue to increase. This is confirmed by their respective radiative forcing values for 2100 in Table 3.6. By 2080 to 2100, these projected changes in emissions levels of short-lived gases and particles contribute a significant portion of the total predicted surface temperature warming for the full A1B scenario; 0.2°C in the Southern Hemisphere, 0.4°C globally, and 0.6°C in the Northern Hemisphere as shown in the time series of yearly average surface temperature change in Figure 3.9.

In Figure 3.10 we examine Northern Hemisphere summer surface temperature change between the 2090s (average over 2091 to 2100) and the 2000s (average over 2001 to 2010) due to the changes in emissions of short-lived gases and particles between the first decade and the last decade of the 21st century. Note the large warming in the Northern Hemisphere mid-latitudes with the major hot spots over the continental United States, Southern Europe and the Mediterranean. Eastern Asia, the region with the strongest radiative forcing due to changes in emissions and loading of short-lived gases and particles, is not one of the hot spots. The mid-latitude warming belt is statistically significant to the 95th percentile, with some regions significant to the 99th percentile. By contrast, the annual-average and seasonal-average patterns of change in precipitation due to changes in emissions of short-lived gases and particles (not shown) are, in general, not statistically significant.

The geographic distribution of radiative forcing is generally less important than the spatial distribution of climate response in predicting climate impact.

We now focus on the large summertime warming over the United States and consider the twenty-first century time series shown in Figure 3.11. By 2100, the change in short-lived gases and particles, primarily the decrease in sulfate and increase in black carbon particles over Asia, contributes ~1.5°C of the total temperature warming of ~4°C predicted for the summertime continental United States when the effects of changes in both short-lived and long-lived gases and particles are included.

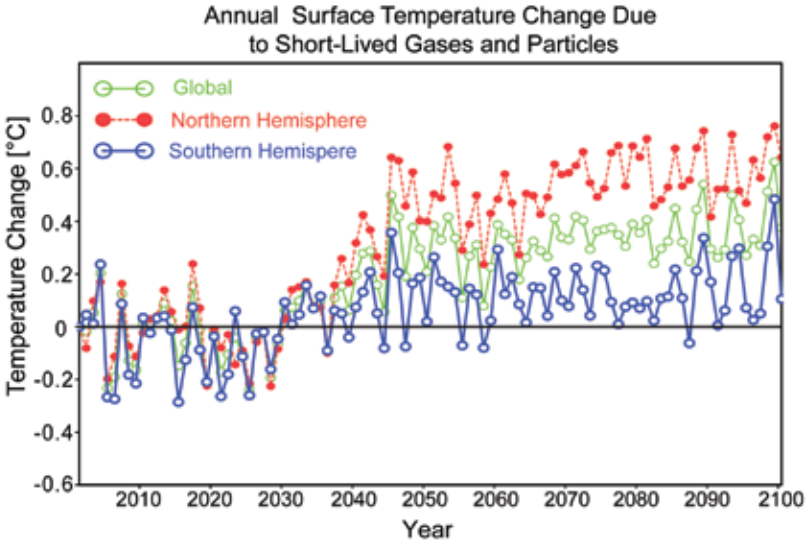

Figure 3.9 Surface temperature change in °C (2000 to 2100) due to short-lived gases and particles in the GFDL model.

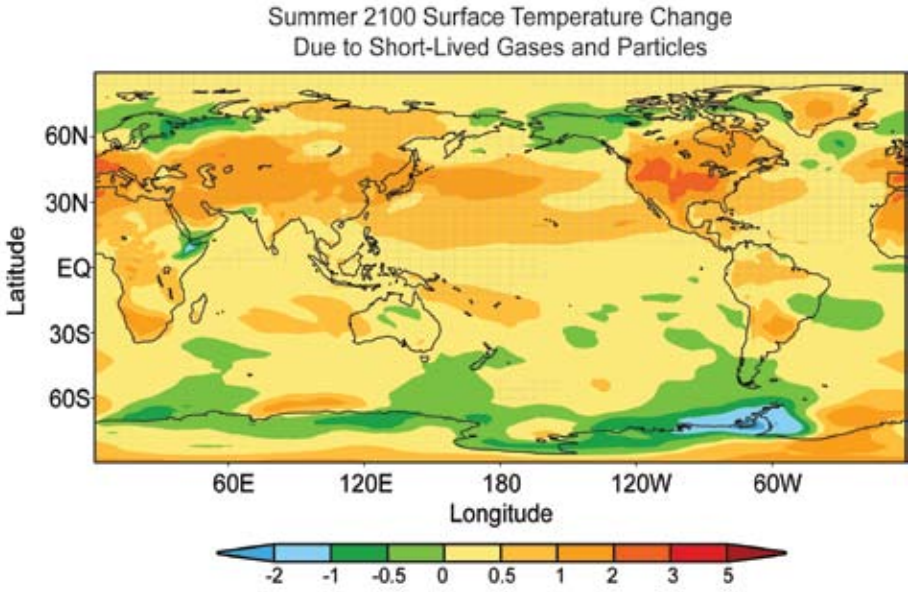

Figure 3.10 Surface temperature change in °C due to short-lived gases and particles during Northern Hemisphere summer for 2100 to 2091 *vs.* 2010 to 2001 in the GFDL model.

Model simulations indicate that short-lived gases and particles could account for a significant portion of the warming in 2100.

In Figure 3.12, we focus more narrowly on the central United States where the strong summertime warming was predicted for 2100. Monthly-mean area-averaged values of temperature, precipitation, and available root-zone soil water are shown for both the full A1B emissions scenario (dashed lines), where both long-lived greenhouse gases and short-lived gases and particles change and the emissions scenario with only long-lived greenhouse gases changing and short-lived gases and particle levels fixed at 2001 values (solid lines). The values are ensemble averages over the last 40 years (2061 to 2100) for each simulation. Here the climate model does predict a statistically significant (at the 95 percent confidence level) decrease in precipitation due to the change in short-lived gases and particles (blue curves in Figure 3.12 and green curve in Figure ES.1). We next consider root-zone soil water, a quantity that integrates and responds to both temperature and precipitation. There is a statistically significant (at the 95 percent confidence level) decrease of up to 50 percent in available root-zone soil water in the Central United States during late summer (July through September), which could have important consequences for United States grain production, and merits future attention. This is the result of a global increase in short-lived gas and particle forcing, located primarily over Asia, which in turn results from the large changes projected by the A1B "marker" scenario for Asian emissions of SO_2 and black carbon.

We also find, as already discussed for year 2050 in Section 3.3.4, that the regional patterns of climate change in 2100, due to changes in emissions of short-lived gases and particles, are the result of regional patterns in the climate system's response rather than regional patterns in radiative forcing. The global patterns of surface temperature change in 2100 are similar for the short-lived gases and particles and the well-mixed greenhouse gases with the strongest surface temperature warming occurring over the summer continental United States and Mediterranean and the winter Arctic, while the major change in radiative forcing is over Asia (Levy *et al.*, 2008). The predicted summertime warming over the United States is greatly enhanced by projected reductions in SO_2 emissions and increased black carbon emissions and the resulting positive radiative forcings over Asia. In the A1B scenario, this is assumed to be the result of Asian decisions addressing their local and regional air quality. The integrated assessment model projections for A1B assume that SO_2 emissions will be reduced in the future in order to improve air quality, but did

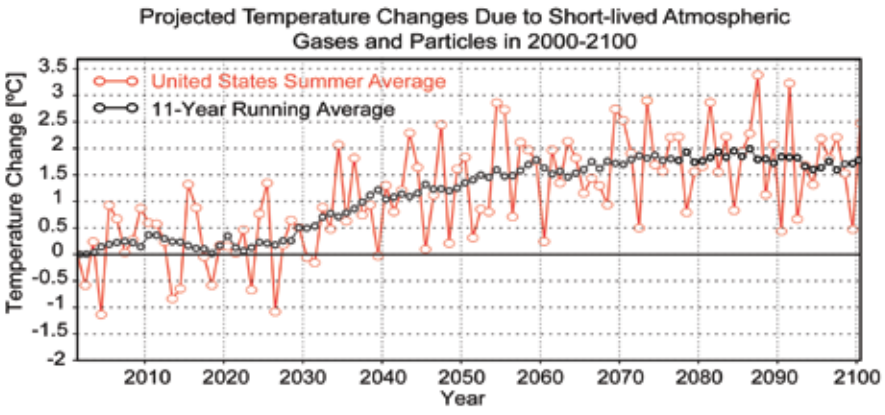

Figure 3.11 Surface temperature change in °C from 2000 over the twenty first century due to short-lived gases and particles over the continental United States during Northern Hemisphere summer in the GFDL model.

not explicitly project carbonaceous particle emissions. Scaling future carbonaceous emissions according to carbon monoxide emissions projections does not lead to similar reductions in emissions of these particles, so that there is an issue of consistency in projecting the influence of future air quality decisions that deserves further study.

3.4 REGIONAL EMISSIONS SECTOR PERTURBATIONS AND REGIONAL MODELS

3.4.1 Introduction to Regional Emissions Sector Studies

An additional set of simulations used global models to examine the impact of individual emissions sectors in specific regions on short-lived gases and particles. This study, in which the GISS and NCAR groups participated, was designed to examine the climate effects of short-lived gases and particles in a more policy-relevant way by focusing on the economic activities that could potentially be subject to regulation or reduction in usage (*e.g.*, by improved efficiency). We look at reductions in total emissions from a given sector in particular regions (North America and Asia), and do not consider any changes in technology or the relative contributions within a sector. As such, these are more useful for assessing the potential impacts of reductions in total power/fuel usage rather than changes in the mix of power generation/transportation types or in emissions control technologies targeted at specific pollutants.

3.4.2 Global Models

The GISS model setup for the regional emissions sector perturbation experiments was the same as that used in the transient climate studies (Section 3.2 and 3.3; see Appendix C and D, sections on Goddard Institute for Space Studies). The NCAR regional/sector perturbation simulations used the CAM-chem model (Lamarque *et al.*, 2005b), in which an updated version of the MOZART chemical transport model (Horowitz *et al.*, 2003) is embedded within the Community Atmosphere Model (CAM3, Collins *et al.*, 2006).

CAM-chem has a representation of tropospheric chemistry with non-methane hydrocarbons (NMHCs) treated up to isoprene, toluene and monoterpenes. The particle simulation in CAM-chem includes the bulk particle mass of black carbon (BC, hydrophobic and hydrophilic), primary organic carbon (POA, hydrophobic and hydrophilic), secondary organic carbon (SOA), ammonium and ammonium nitrate, and sulfate particles. Further details on the CAM-chem model are found in Appendix C in the section on National Center for Atmospheric Research.

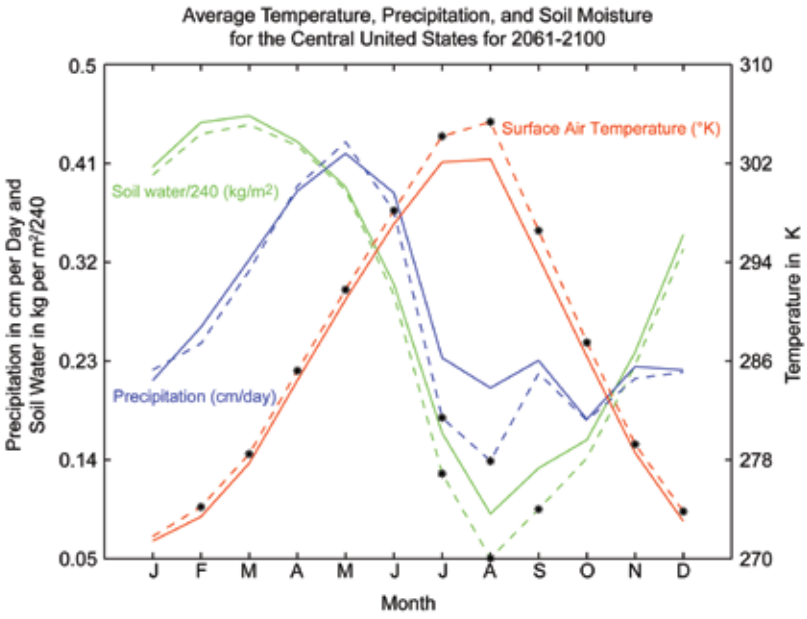

Figure 3.12 Monthly-mean time-series of available root-zone soil water (green lines, scaled by a factor of 1/240 for plotting purposes), precipitation (blue lines), and two-meter air temperature (red lines), averaged over the Central United States (105 to 82.5°W longitude; 32.5 to 45°N latitude). Dashed lines are for the ensemble mean of the A1B experiments, averaged over the years 2061 to 2100; solid lines are for the ensemble mean of the A1B* experiments, also averaged over the years 2061 to 2100. The asterisks represent those A1B monthly average values that are different from their companion A1B* values at the 95 percent confidence level. Temperature in K equals temperature in °C plus 273.15.

3.4.3 Impact of Emissions Sectors on Short-Lived Gases and Particles

This set of experiments consisted of six simulations each reducing the present-day emissions by 30 percent in one sector for one region. By using present-day emissions, the results are not tied to any particular scenario. For present-day emissions, the IIASA 2000 inventory, based on the 1995 EDGAR 3.2 inventory extrapolated to 2000 using national and sector economic development data, was used (Dentener *et al.*, 2005), as in the GISS simulations described above. The exception to this is biomass burning emissions, which are taken from the Global Fire Emission Database (GFED) averaged over 1997

to 2002 (Van der Werf *et al.*, 2003) with emission factors from Andreae and Merlet (2001) for particles. The regions were defined as North America (60 to 130°W, 25 to 60°N) and Asia (60 to 130°E, 0 to 50°N) and the economic sectors defined according to the IIASA inventory as the domestic sector, the surface transportation sector, and a combined industry and power sector (the CAM-chem model did not perform the transportation sector simulations).

A control run with no perturbations was also performed to allow comparison. The goal of these simulations was to calculate the radiative forcing from all the short-lived gases and particles to identify the relative contribution of the given economic sectors in these two regions. This complements prior work examining the response to a subset of the gases and particles included here (*e.g.,* Koch *et al.*, 2007; Unger *et al.*, 2008). As the forcings were expected to be small, we concentrate on simple metrics rather than the climate response. The CAM-chem model did not calculate radiative forcing, so we also use aerosol optical depth, which is a good indicator of the radiative forcing from particles. All simulations were 11-year runs, with analysis performed over the last ten years.

The simulations were not performed using a full methane cycle, but the methane response to the imposed perturbations can be estimated by examining the changes in methane's oxidation rate. In these simulations, methane was prescribed at present-day values. Thus any change in methane oxidation is due solely to changes in the abundance of oxidizing agents. The difference in the steady-state abundance of methane that would occur as a result of this oxidation change is a simple calculation ($[CH_4]'/[CH_4] = L/L'$ for the global mean where L is the methane loss rate and the "prime" notation indicates the adjusted amounts). Use of the model's oxidation rate in the perturbation runs fully captures spatial and seasonal variations, and thus provides an accurate estimate of the equilibrium response of methane to the emissions changes. Finally, the radiative forcing resulting from these indirect methane changes is calculated using the standard formulation (Ramaswamy *et al.*, 2001).

We first examine the global mean annual average radiative forcing in the GISS model from the regional perturbations and those by economic sectors (Table 3.10). The effect of the

Table 3.10 Radiative forcing in milliWatts per square meter (mW per m²), from regional emission sector perturbations in the GISS model.

Region	Sector	Sulfate	BC	OC	Nitrate	Ozone	Methane (indirect)	All
North America	Domestic	0	-3	2	1	2	1	4
	Surface Transportation	-3	-5	0	1	-5	4	-9
	Industry/power	14	-2	-1	0	5	2	18
Asia	Domestic	0	-42	13	1	-12	-2	-41
	Surface Transportation	2	-8	1	2	-5	7	-2
	Industry/power	13	-4	0	-1	-1	5	12

Perturbations are 30 percent reduction in emissions of all species from the indicated economic sector in the given region. Direct forcings are shown for sulfate, black carbon (BC), organic carbon (OC), nitrate, and ozone. The effect of ozone precursor species on methane is included as methane "indirect". Note that particle indirect effects are not included.

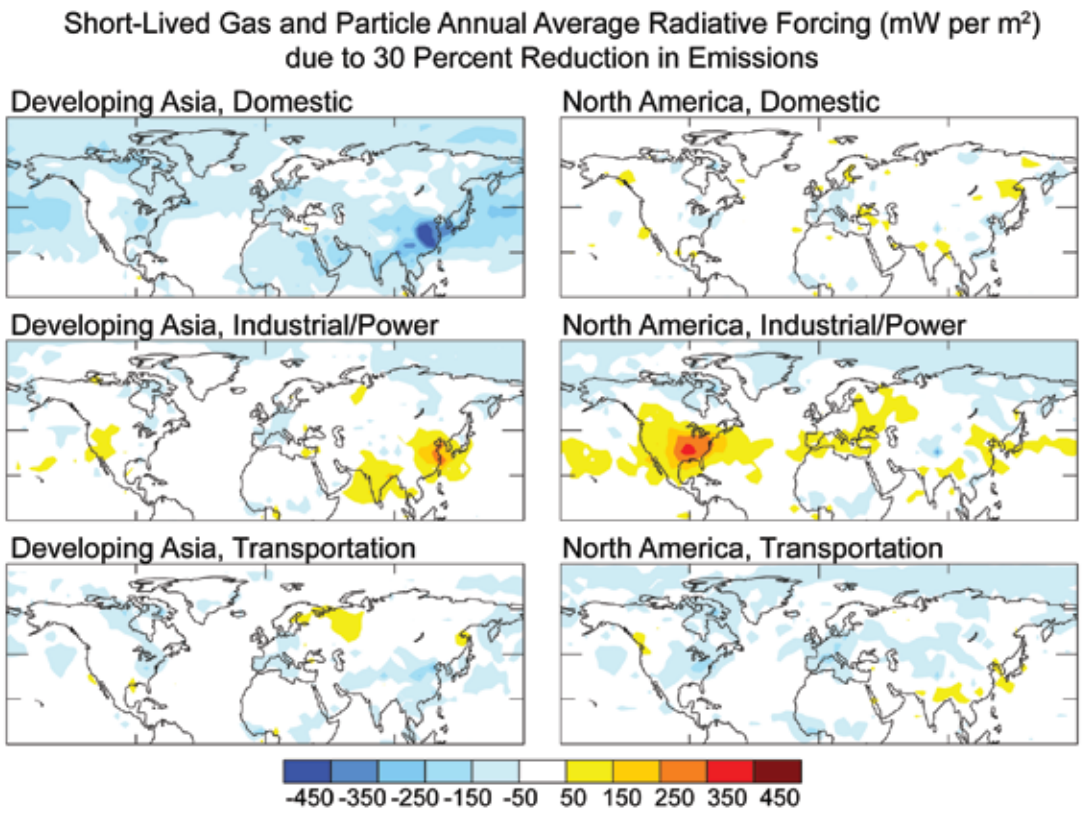

Figure 3.13 Short-lived gas and particle annual average radiative forcing (mW per m^2) due to 30 percent reductions in emissions from the given region and economic sector in the GISS model.

perturbations is generally larger for Asian than for North American emissions. The only radiative forcing from an individual gas or particle to exceed 10 milliWatts per square meter (mW per m^2) from a North American perturbation is the sulfate forcing from a reduction in industrial/power emissions. In contrast, forcings from sulfate, black carbon, organic carbon and ozone all exceed 10 mW per m^2 in response to perturbations in developing Asia, with the largest response for reductions in black carbon when domestic emissions are reduced (-42 mW per m^2). The spatial pattern of the radiative forcing is also shown (Figure 3.13).

The two largest net forcings are in response to changes in North American industrial/power emissions, whose forcing is positive and is dominated by reductions in forcing from sulfate, and the Asia domestic sector, whose forcing is negative and dominated by reductions in black carbon and ozone. The spatial pattern of the aerosol optical depth changes capture the bulk of the radiative forcing in these two cases (Figure 3.14 *vs*. Figure 3.13). The sign is opposite, however, in the case of industrial/power emissions as these are dominated by reflective sulfate particles, so decreased aerosol optical depth causes positive radiative forcing.

The GISS and CAM-chem models show very similar patterns of aerosol optical depth changes for these two perturbation experiments. For emissions reduction in the Asia domestic sector, the global mean aerosol optical depth decreases by 0.15 in the GISS model and 0.13 in the CAM-chem model, while for the North American industrial/power sector the decreases are 0.09 and 0.13, respectively. Hence the particle response appears to be fairly robust across these two models. Results suggest that the calculation of radiative forcing from aerosol optical depth introduces an additional inter-model difference that is less than that from the aerosol optical depth calculation (Schulz *et al.*, 2006), so that the total inter-model variation in radiative forcing from particles is probably on order of 50 percent. Results for ozone show marked differences, however, with the response of the tropospheric ozone column in the GISS model nearly always a factor of two to three greater than in the CAM-chem model. We believe that these differences primarily reflect the

The effect of the perturbations is generally larger for Asian than for North American emissions.

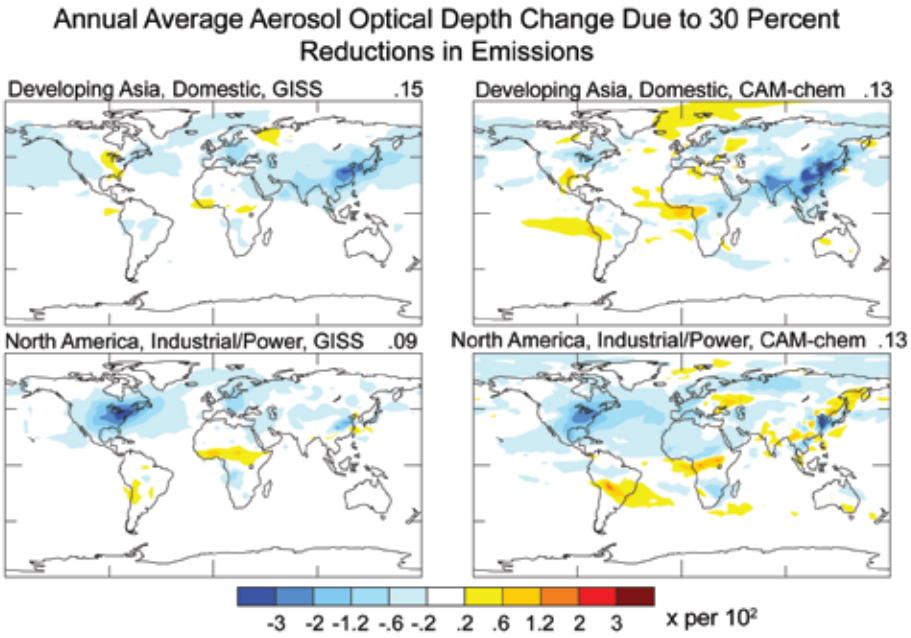

Figure 3.14 Annual average aerosol optical depth change due to 30 percent reductions in emissions from the given region and economic sector in the GISS (left column) and CAM-chem (right column) models. Values in the upper right give the global mean.

In most cases, substantial reduction in surface particle concentrations result from the regional economic sector emissions reductions. This is especially so in the Asia domestic analysis.

inclusion of the stratosphere in the GISS model, which leads to enhanced forcing as ozone near the tropopause has a particularly large radiative impact. Hence, the ozone radiative forcing is not yet robust to inter-model differences. However, particles typically have a larger influence on climate than ozone, so that the net radiative forcing remains a relatively more robust quantity.

We also examine changes in surface pollution levels in these simulations. Changes in surface ozone are typically small, with annual average local reductions of up to about 1 to 1.5 parts per billion by volume (ppbv) in both the CAM-chem and GISS models in response to reduction in transportation or industrial/power emissions. These increase to levels of 1 to 3 ppbv during boreal summer. Both these annual and summer increases are statistically significant. Changes in particles are larger. In most cases, substantial reduction in surface particle concentrations result from the regional economic sector emissions reductions. This is especially so in the Asia domestic analysis, where summer sulfate concentrations are lowered by 100 to 250 parts per trillion by volume (pptv) locally, and black carbon concentrations drop by 1800 to 2000 pptv for both summer and annual averages. Smaller air quality improvements are also clear in the response to industrial/power and transportation emissions reductions in both regions. These reductions in particles are generally quite similar in the two models, with differences of only 5 to 20 percent in most cases.

The analysis shows that reductions in surface transportation emissions have a net negative forcing from short-lived gases and particles in both regions, primarily due to reductions in ozone and black carbon. As these are both pollutants at the surface, reducing emissions transport offers a way to simultaneously improve human health and mitigate climate warming (though the climate impact is quite small for Asia). The total climate mitigation would of course be larger adding in the effect of reduced emissions of long-lived greenhouse gases. In contrast, industrial/power sector emissions have their largest effect on climate through sulfate, and hence yield a positive forcing. Thus, the net effect of changes in short-lived gases and particles to industrial/power emissions reductions will offset a portion of any climate benefit from reduced emissions of long-lived gases. The domestic sector presents a similar picture to that seen for surface transportation. The effects are substantially larger in Asia, however. Hence, reductions in domestic emissions from Asia

Table 3.11 Total short-lived gas and particle radiative forcing (in mW per m^2) as in Table 3.10 but for summer (June through August).

Region	Sector	Total forcing
North America	Domestic	6
	Surface Transportation	-10
	Industry/power	34
Asia	Domestic	-69
	Surface Transportation	-3
	Industry/power	10

Perturbations are 30 percent reduction in emissions of all species from the indicated economic sector in the given region. Direct forcings are shown for sulfate, black carbon (BC), organic carbon (OC), nitrate, and ozone. The effect of ozone precursor species on methane is included as methane "indirect". Note that particle indirect effects are not included.

offer another means to improve human health and mitigate warming. Note that the effects become particularly strong in Northern Hemisphere summer (Table 3.11), offering a potential path to mitigate increased summer heat over the Northern Hemisphere continents.

Overall, the Asia domestic emissions offer the strongest leverage on climate via short-lived gases and particles. This is partially a result of their magnitude, and partially their occurrence at lower latitudes than North American (or European) emissions. This enhances their impact as photochemistry is faster and incoming radiation is more abundant at lower latitudes. Perturbing the Asia domestic sector in the IIASA 2000 emissions inventory used here yields a much greater effect via black carbon changes than via sulfate changes. This reflects the influence of domestic fuel usage, for which black carbon is the dominant emission, and hence reductions from emissions in this sector in particular seem attractive for warming mitigation. As domestic usage and emissions are extremely difficult to quantify in the developing world, further studies of this sector are especially needed to characterize the uncertainty in these emissions. The GISS and CAM-chem results differ in the magnitude of the aerosol optical depth change resulting from the Asia domestic sector perturbations by only 13 percent, and this sector/region has the largest influence in both models for both radiative forcing and surface pollution. The stronger aerosol optical depth response in the CAM-chem model suggests that the radiative forcing in that model might be even larger than the 50 mW per m^2 global mean annual average seen in the GISS results.

Further work is required to more thoroughly characterize the robustness of these conclusions across a larger number of models, to explore the impact of particle indirect effects on clouds, and to examine alternative emissions scenarios considering changes in the mix of sources constituting a given sector and the influence of potential technological changes. The latter could be designed to reduce emissions of particular pollutants, while not affecting others. Our results for the radiative forcing from individual gases and particles give an idea of the potential impact of such technologies. However, we note that these technologies could also have effects on overall fuel consumption by altering the efficiency of a particular process.

Overall, the Asia domestic emissions offer the strongest leverage on climate via short-lived gases and particles. This is partially a result of their magnitude, and partially their occurrence at lower latitudes than North American (or European) emissions.

Interestingly, both the transient climate projections and the present-day perturbations find that emissions from Asia are the most important controllers of climate trends or mitigation. Given that the radiative forcing reduction from decreases in Asia domestic emissions extends over much of the Northern Hemisphere (Figure 3.13), and the conclusion from the transient

climate simulations that the climate response to short-lived gas and particle changes is not closely localized near their emissions, it seems plausible that emissions from this region may have as large or larger an effect on other parts of the Northern Hemisphere as changes in local emissions.

3.4.4 Regional Downscaling Climate Simulations

The sector-based simulations presented in Section 3.4.3 suggest that reductions in surface level ozone or black carbon would have a negative radiative forcing, while reductions in sulfate particles from the utility sector would have a positive radiative forcing. If concentration levels for ozone and small-diameter particles ($PM_{2.5}$)[6] exceed threshold standards under the United States Clean Air Act, emissions control strategies must be developed. Since these levels vary spatially and are affected by local emissions, regional scale models are needed to develop the emissions control strategies that meet these standards at county and state levels. To achieve reductions in small-diameter particles, emissions scenarios often include utility sector emissions reductions to lower sulfate particle levels. As shown in the previous section, lowering sulfate particle concentrations could actually have negative implications for radiative forcing and climate temperature increases. Regional downscaling studies shown in this section suggest that future changes in regional climate could reduce the benefits from anticipated emissions reductions on lowering ozone.

Downscaled regional scale climate simulations (*e.g.*, Leung and Gustafson, 2005; Liang *et al.*, 2006; Liang *et al.*, 2004) rely on a global climate model to provide boundary conditions for the regional domain as well as the radiative effect of well-mixed greenhouse gases within the domain for the radiation calculations. Regionally downscaled climate simulations are needed by a number of applications that must consider local changes in future climate. Since ozone and small particles exceedances of regulatory thresholds are substantially affected by local scale changes in emissions and meteorology, several recent studies using regionally downscaled climate scenarios have been used to study the sensitivity of air quality to potential changes in future climate. The primary purpose of these studies was to study how increases in temperature and other future climate changes could affect ozone and small-diameter particles and potentially decrease the effectiveness of anticipated emissions reductions.

Downscaled regional climate model simulations by Gustafson and Leung (2007) and Nolte *et al.* (2008) have used the EPA/NOAA air pollution model to test the impact of future (*ca.* 2050) climate on ozone and particles with current emissions scenarios. Biogenic emissions, which are meteorologically dependent, were recalculated

[6] $PM_{2.5}$ are all small particles with diameters less than 2.5 micrometers

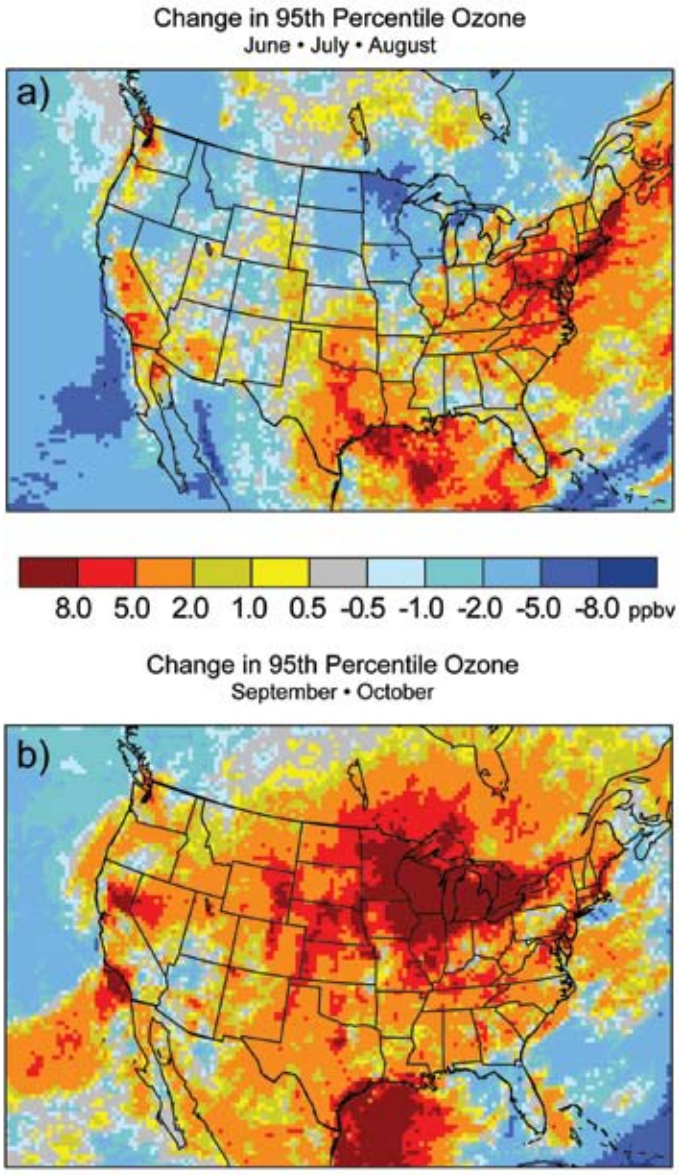

Figure 3.15 From Nolte *et al.* (2008), the change in ozone at the upper end of the ozone distribution (average of the ≥95th percentile values for each grid) for (2050 to present) years of simulation under A1B regional climate model simulations.

under the future climate scenario. Results suggest that future climate changes could increase maximum ozone levels by approximately ten percent in some regions (Figure 3.15). With anticipated emissions reductions under United States Clean Air Act requirements, these results suggest that future climate could dampen the effectiveness of these emissions controls. Evaluation of ensemble regional climate model results are essential for this application before quantitative conclusions can be made about the impact of future climate on specific emissions control strategies; however, these results suggest that climate change is a factor that needs to be considered in air quality management.

These regional downscaling climate studies rely on climate forcing linkages from global climate simulations with future trends for long-lived gases including CO_2, CH_4, N_2O, and halocarbons. The influence of short-lived gases and particles on future climate has not been included in those studies to date; however, more recent developments are underway to include direct and indirect radiative effects in the regional chemistry model. Based on the known positive radiative forcing effect of ozone, the increases in ozone in response to future climate in Figure 3.15 should have a positive radiative forcing that could dampen the net negative radiative forcing anticipated from future emissions reductions for ozone (Section 3.4.3).

While regional downscaling climate impacts from short-lived gases and particles cannot be directly reported on, future emissions scenarios were considered by several regional downscaling studies for the purpose of air quality impacts under future climate. The impact of climate only and then an emissions change scenario were tested by Nolte *et al.* (2008) and Hogrefe *et al.* (2004). As presented in Figure 3.15, results looking only at the climate change without future changes in emissions suggest that future climate changes could increase maximum ozone levels by approximately eight ppbv or ten percent in some regions of North America. Looking at future emissions scenarios for nitrogen oxides and sulfur dioxide reductions demonstrates that the uncertainty in the future emissions scenarios

Climate change itself could have a significant impact on low-level ozone concentrations, leading to yet further changes in climate.

introduces a much larger variation in the air quality conclusions depending on the scenario (Hogrefe *et al*., 2004; Nolte *et al.*, 2008). Similar to the findings here about short-lived gases' and particles' impact on climate, the range of plausible air quality impacts from future emissions scenarios suggest very different outcomes, and the future scenarios of emissions for short-lived gases and particles have a great deal of obvious, inherent uncertainty.